Research Square

Preprints are preliminary reports that have not undergone peer review.
They should not be considered conclusive, used to inform clinical practice,
or referenced by the media as validated information.

Clincelin: A redesigned lincosamide with enhanced intracellular accumulation and adaptive binding to resistant ribosomes

Gabriela Balíková Novotná

gnovotna@biomed.cas.cz

Institute of Microbiology CAS; BIOCEV https://orcid.org/0000-0002-5464-4763

Michaela Novotná

Institute of Microbiology, Czech Academy of Sciences https://orcid.org/0000-0001-5068-8454

Petr Slavík

SigutLabs s.r.o. https://orcid.org/0000-0002-3326-6169

Fanny Demay

Institute of Microbiology, Czech Academy of Sciences

Durga Mahor

Institute of Microbiology CAS; BIOCEV

David Řeha

IT4Innovations, VSB – Technical University of Ostrava

Fanny Boissier

INSERM U1212 Acides nucléiques: Régulations Naturelle et Artificielle (ARNA), Institut Européen de Chimie et Biologie, Université de Bordeaux

Julie Pokorná

Institute of Microbiology, Czech Academy of Sciences https://orcid.org/0009-0004-4878-1851

Vladimir Vimberg

Institute of Microbiology of the Academy of Sciences

Marie Brajerová

Department of Medical Microbiology, Second Faculty of Medicine, Charles University and Motol University Hospital

Tommaso Stefani

Institute of Microbiology, Czech Academy of Sciences

Jakub Svoboda

Institute of Biotechnology, Czech Academy of Sciences

Radek Gazak

Institute of Microbiology

Michal März

SigutLabs s.r.o. https://orcid.org/0000-0002-5712-1503
Jan Hošek
SigutLabs s.r.o.
Markéta Koběrská
Institute of Microbiology of the CAS https://orcid.org/0000-0002-9787-4227
Vaclav Eigner
Institute of Physics ASCR https://orcid.org/0000-0003-1014-3980
Lada Hanzlikova
Institute of Microbiology of the Czech Academy of Sciences
Marek Kuzma
Institute of Microbiology https://orcid.org/0000-0001-7415-2734
Marcela Krůtová
Department of Medical Microbiology, Second Faculty of Medicine, Charles University and Motol University Hospital
Zdeněk Kameník
Institute of Microbiology, Czech Academy of Sciences
Kryštof Šigut
SigutLabs s.r.o.
Jiri Janata
Institute of Microbiology, The Czech Academy of Sciences https://orcid.org/0000-0002-4582-2062
C. Innis
INSERM https://orcid.org/0000-0003-3153-9490

Article

Keywords:

Posted Date: February 25th, 2026

DOI: https://doi.org/10.21203/rs.3.rs-8873829/v1

License: This work is licensed under a Creative Commons Attribution 4.0 International License.
Read Full License

Additional Declarations: Yes there is potential Competing Interest. The authors R.G., Z.K., and J.J. are named inventors on patent applications WO2018161979 and US20200017537 “Lincosamide derivatives, preparation and use thereof as antimicrobial agent” filed by the Institute of Microbiology CAS, covering the lincosamide derivatives and their antimicrobial uses described in this study. All other authors declare no competing interests.

Abstract

Lincosamides are an important class of clinically used antibiotics that inhibit translation by binding to the peptidyl transferase center of the ribosome. However, their efficacy is impaired by the widespread acquisition of genes coding for erythromycin resistance methyltransferase (Erm), which confer resistance by dimethylating adenine A2058 in the 23S ribosomal RNA. Here, we report clincelin, a novel chimeric lincosamide that retains conserved lincosamide thiooctose core and integrates structural features from two natural antibiotics—a propylated proline from lincomycin and salicylate from celesticetin—together with additional clinically validated C7 chlorination. Biochemical and cellular analyses revealed that the presence of salicylate and chlorination synergistically enhances intracellular accumulation, giving clincelin greater antibacterial activity than the parent compounds and the clinically used clindamycin. Notably, clincelin partially retains its efficacy against *erm*-mediated resistant pathogens, which is explained by cryo-electron microscopy showing that the salicylate moiety adopts distinct binding modes on drug-sensitive versus A2058-dimethylated *Staphylococcus aureus* ribosomes. Altogether, a comprehensive functional understanding of lincosamide structural modifications will enable the development of novel agents designed to overcome existing resistance.

Main

The global rise of antibiotic-resistant bacterial strains demands urgent action to address this escalating health crisis (World Health Organization, 2023). While developing new antibiotics is a lengthy and expensive process, modifying existing ones presents a more immediate solution. Lincosamides, a class of antibiotics targeting the peptidyl transferase center (PTC) of the bacterial ribosome (Fig. 1A-C), have shown promise in overcoming resistance mechanisms if suitably modified (Mitcheltree et al., 2021; Wu et al., 2024). Expanding the diversity of lincosamide modifications and elucidating the mechanisms behind their enhanced activity increases the likelihood of developing refined clinical agents to combat escalating antibiotic resistance.

Lincomycin, celesticetin, and Bu-2545 are the only naturally occurring lincosamides identified to date (Hoeksema H. et al., 1954; DeBoer et al., 1955; Hoeksema et al., 1964; Hoeksema, 1968; Hanada et al., 1980). These compounds share a conserved structural scaffold composed of a thiooctose linked to either *N*-methyl-4-propyl-L-proline (lincomycin) or *N*-methyl-L-proline (celesticetin and Bu-2545), with celesticetin uniquely carrying an additional salicylate moiety (Fig. 1D). Structural studies have consistently demonstrated that conserved interactions between the thiooctose and 23S rRNA underlie ribosome binding across lincosamide variants (Fig. 1B,C) (Schlünzen et al., 2001; Mitcheltree et al., 2021; Paternoga et al., 2023; Wu et al., 2024). The *N*-methyl-4-propyl-L-proline moiety (hereafter referred to as propyl proline) is a key determinant of antimicrobial activity, as it obstructs proper accommodation of the A-site tRNA acceptor stem within the PTC (Schlünzen et al., 2001; Tu et al., 2005; Dunkle et al., 2010). The semi-synthetic derivative clindamycin, generated from lincomycin by C7 chlorination, exhibits markedly enhanced antibacterial activity, enabling its clinical application; however, the precise molecular basis for this improvement remains unresolved (Matzov et al., 2017). Moreover, the higher activity of

celesticetin relative to Bu-2545 (Magerlein, 1971; Hanada et al., 1980; Kadlčík et al., 2017) suggests that the salicylate substituent—although positioned distal to the PTC— further contributes to antibacterial efficacy. The underlying mechanism is likewise unclear.

Resistance to lincosamides often arises through Erm-mediated methylation of the ribosomal RNA, which hinders antibiotic binding (Leclercq and Courvalin, 1991; Toh et al., 2007). However, recent research has demonstrated that modified lincosamides, such as iboxamycin and cresomycin, can overcome such resistance by enhanced binding affinity that compensates for the lost interactions (Mitcheltree et al., 2021; Wu et al., 2024).

In our previous work, we developed two lincosamide chimeras, celin and OD-Celin (ODC), that merge structural elements of lincomycin and celesticetin scaffolds (Fig. 1D) and display substantially improved antibacterial potency compared to lincomycin (Kadlčík et al., 2017). Building on this framework, we now report the development and multigram synthesis of clincelin (CLC), produced by C7 chlorination of ODC in direct analogy to the lincomycin–clindamycin pair (Fig. 1D). Both ODC and CLC display broadly improved antibacterial potency arising mainly from improved intracellular accumulation, with CLC additionally attenuating resistance mediated by Erm methyltransferases and ABC-F ribosomal protection proteins. Moreover, our cryo-EM studies reveal the CLC's unique ability to bind to Erm-methylated ribosomes by forming an alternative contact between its salicylate moiety and the ribosome.

Results

Synthesis of artificial chimeric antibiotics ODC and CLC

To access ODC and CLC in multigram quantities—exceeding yields previously achieved by combinatorial *in vitro* biosynthesis (Kadlčík et al., 2017)—we established a synthetic route inspired by the work of Vasella and colleagues (Collin et al., 2009) (Fig. 1E). Starting from lincomycin A, sequential protection, oxidation, and selective reduction afforded a key intermediate suitable for subsequent thiol side-chain incorporation. Final deprotection and esterification with salicylic acid yielded ODC, which was obtained in good purity with an overall yield of 19% from lincomycin A and further purified by crystallization. Conversion of ODC to the chlorinated analogue CLC proceeded in high yield (93%) via oxalyl chloride–mediated activation followed by base treatment. Further details about the synthesis are provided in the Supplementary Information. All intermediates were prepared on a multigram scale, and both final compounds were fully characterized. The solid-state structure of CLC was determined by single-crystal X-ray diffraction at 0.82-Å resolution (Supplementary Fig. 1), confirming the expected molecular architecture.

Chimeric lincosamides ODC and CLC exhibit improved antimicrobial properties compared to lincomycin and clindamycin

To evaluate the therapeutic potential of the chimeric lincosamides ODC and CLC, we performed a comparative *in vitro* susceptibility analysis against an extensive panel of multidrug-resistant clinical isolates.

Gram-negative pathogens typically exhibit intrinsic resistance to lincosamides due to the synergistic effect of the outer membrane permeability barrier and active efflux mediated by the AcrAB-TolC multidrug transport system (Pérez et al., 2007; Jang, 2023). While all tested lincosamides maintained characteristically low activity against wild-type Gram-negative pathogens, the critical role of efflux was confirmed using a TolC-deficient *Escherichia coli* BW25113 strain. In this mutant background, CLC, which combines chlorination with salicylate attachment, exhibited an 8- to 16-fold increase in potency relative to clindamycin, and a 256- to 512-fold increase compared to lincomycin (Supplementary Fig. 2). These data suggest that chimeric lincosamides remain substrates for the AcrAB-TolC efflux system in Gram-negative bacteria.

The chimeric lincosamides ODC and CLC exhibited superior antibacterial potency against Gram-positive clinical isolates compared to lincomycin and clindamycin. Notably, CLC emerged as the most potent derivative, consistently circumventing several established resistance phenotypes (Fig. 2A).

Beyond its enhanced baseline activity against susceptible isolates, CLC effectively bypassed resistance mediated by ABC-F proteins VgaA/B, LsaA, and CplR (Fig. 2A). These proteins typically confer resistance to lincosamides, streptogramins A and pleuromutilins through a ribosomal protection mechanism that displaces the drug from its binding (LS_AP phenotype) (Sharkey et al., 2016; Crowe-McAuliffe et al., 2021; Obana et al., 2023). Furthermore, CLC maintained its activity against isolates harboring Erm-type 23S rRNA methyltransferases. These enzymes catalyze the N6, N6-dimethylation of the conserved A2058 residue (*E. coli* numbering), a modification that sterically hinders the binding of macrolide, lincosamide, and streptogramin B antibiotics (the MLS_B phenotype). While *erm* expression can be either constitutive or macrolide-inducible, lincosamides typically fail to serve as inducers of *erm* expression. Consequently, both ODC and CLC effectively bypass inducible resistance, maintaining high potency against these strains. More importantly, CLC exhibited a 16- to 256-fold increase in potency relative to clindamycin (Fig. 2A, Supplementary Fig. 2). By contrast, both ODC and CLC showed only marginal activity against strains carrying the Cfr 23S rRNA methyltransferase, which methylates adenine at position 2503 and mediates $PhLOPS_A$ resistance to phenicols, lincosamides, oxazolidinones, pleuromutilins, and streptogramin A (Fig. 2A).

Following the evaluation of the general clinical panel, we focused on *Clostridioides difficile*, a leading cause of healthcare-associated infections (He et al., 2012) and a pathogen where traditional lincosamide therapy is contraindicated. Clindamycin exposure is a primary risk factor for *C. difficile* infection (CDI) because it disrupts the protective gut microbiota while failing to suppress *C. difficile* due to its intrinsic and acquired resistance (Johnson et al., 1999; Pear et al., 2000; Kuijper et al., 2001; Buffie et al., 2012). The intrinsic resistance was recently attributed to the ABC-F protein CplR (Obana et al., 2023).

Given CLC's ability to circumvent ABC-F-mediated resistance, we evaluated its broad-spectrum efficacy against a phylogenetically diverse panel of *C. difficile* clinical isolates from Eastern Europe (Plankaová et al., 2023; Krůtová et al., 2025; Zíková et al., 2025). This collection spans five major phylogenetic clades (Knight et al., 2021), representing the global diversity of the species and capturing the natural variation in CplR variants. Our results show that CLC consistently outperformed clindamycin across all phylogenetic groups, with significantly lower MIC values (Fig. 2B). By overcoming CplR-mediated ribosome protection, CLC addresses a critical limitation of the lincosamide class and potentially offers a more effective alternative for treating infections, where clindamycin-resistant *C. difficile* remains a therapeutic obstacle.

ODC and CLC inhibit the initiation step of bacterial translation

To determine whether ODC and CLC target bacterial translation analogously to other lincosamides, we used a toeprinting assay for locating stalled ribosomes on two distinct model mRNAs previously used in similar studies (Orelle et al., 2013; Mitcheltree et al., 2021). In the assay, commercially available PURExpress Δribosomes translation system (NEB) was reconstituted with in-house purified ribosomes from *Staphylococcus aureus* JE2. This hybrid *E. coli*/*S. aureus* system was previously established for compatibility of the translational machineries (Gupta et al., 2013). Further, we used mRNA templates containing the $ermBL_V$ (Seip et al., 2018) and $ermDL_V$ ORFs, in which an isoleucine codon was introduced to trap ribosomes that were not inhibited by the antibiotic, as the treatment of the reaction with mupirocin prevents aminoacylation of $tRNA^{Ile}$ and consequently causes ribosomes to stall at isoleucine codons.

Treatment with 5 μM celesticetin, lincomycin, clindamycin, ODC, and CLC resulted in ribosomal stalling at the AUG start codon of both open reading frames. In contrast, no or little ribosome accumulation was observed in the absence of the tested antibiotic, suggesting that these compounds inhibit the formation of the first peptide bond (Fig. 3C,D). At this concentration, which is above the MIC of the respective *S. aureus* JE2 strain for all tested lincosamides except celesticetin (Fig. 3A), all propyl proline-containing lincosamides lincomycin, clindamycin, ODC, and CLC achieved complete translation inhibition. In contrast, celesticetin, lacking the propyl side chain at the proline moiety, caused only partial inhibition, allowing a subset of ribosomes to bypass the AUG stalling site and reach the trap codon.

CLC displays superior intracellular accumulation and improved in vitro activity against A2058-dimethylated ribosomes

To dissect the mechanism underlying the increased potency of CLC relative to clindamycin, we first compared activities of celesticetin, lincomycin, clindamycin, ODC, and CLC in a transcription-translation (TX-TL) assay utilizing cell-free lysate derived from lincosamide-sensitive *S. aureus* RN4220 (Kwon and

Jewett, 2015; Silverman et al., 2019). Except for celesticetin, which exhibits significantly lower potency to inhibit translation of the mAmetrine fluorescence reporter (IC_{50} ~0.74 μM), all other antibiotics displayed surprisingly nonsignificant differences relative to clindamycin (IC_{50} ~0.13 μM) (Fig. 4A) despite their different antibacterial activities (Figs. 2 and 3A). This suggests that the chlorine atom and salicylate moiety attached to the lincosamide core do not directly interfere with bacterial translation. Interestingly, an *in vitro* competitive displacement assay showed that clindamycin, but not CLC, displaced lincomycin from its binding site on *S. aureus* JE2 ribosomes, indicating that clindamycin has a higher affinity for staphylococcal ribosomes than CLC (Fig. 4B).

Since none of the previous *in vitro* testing explained CLC's enhanced antimicrobial potency, we further assessed the intracellular accumulation of lincomycin, clindamycin, ODC, and CLC in *S. aureus* using liquid chromatography-mass spectrometry (LC-MS) (Iyer et al., 2018) (Fig. 4C). Notably, the LC-MS analysis revealed distinct accumulation profiles among the analogues: clindamycin and ODC both exhibited approximately 2-fold higher intracellular concentrations than lincomycin. Of note, CLC demonstrated superior intracellular accumulation exceeding clindamycin levels by more than 3-fold. A similar trend was observed in both the lincosamide-sensitive strain JE2 and its lincosamide-resistant counterpart, constitutively expressing the *ermB* methyltransferase gene (strain NE854). These data indicate that the enhanced antibacterial activity of CLC is primarily driven by optimized intracellular pharmacokinetics. Furthermore, because the accumulation of CLC significantly exceeds the combined incremental gains of the chlorinated (clindamycin) and salicylated (ODC) derivatives, the dual modification appears to exert a synergistic effect on cellular uptake or retention.

To elucidate the molecular basis for CLC's improved efficacy against resistant strains, we repeated the toeprinting analysis across a broad antibiotic concentration gradient using both sensitive and A2058-dimethylated ribosomes. The latter were purified from *S. aureus* NE1858, which constitutively expresses the *ermB* methyltransferase (Fig. 4D,E). Irrespective of the distinct antibacterial potencies (Fig. 3A), lincomycin, clindamycin, ODC, and CLC inhibited *in vitro* translation by sensitive ribosomes to a similar extent, with complete stalling achieved at 5 μM (Fig. 4D,E). The uniform inhibition of sensitive ribosomes is consistent with CLC's superior potency arising from enhanced intracellular accumulation rather than increased ribosomal affinity. In contrast, we observed pronounced differences in stalling efficiency of A2058-dimethylated ribosomes, despite primer extension inhibition analysis indicated that only ~60% of the ribosome population carried the dimethyl modification (Extended Data Fig. 6C). In this modified ribosomal pool, lincomycin failed to achieve complete translation inhibition even at 500 μM, with ribosomes bypassing the stalling site and reaching the trap codon. In contrast, both clindamycin and ODC achieved full inhibition at this concentration, while CLC demonstrated superior biochemical potency, reaching complete inhibition at only 50 μM.

Collectively, these findings indicate that the enhanced antibacterial potency of CLC against sensitive strains is primarily driven by its markedly improved intracellular accumulation, which increases the effective drug concentration within the cell. Furthermore, its efficacy against resistant strains appears to be a dual consequence of this superior accumulation and a 10-fold more effective inhibition of A2058-

dimethylated ribosomes compared to clindamycin. This suggests that the structural modifications in CLC not only facilitate cellular entry but also provide a capacity to bypass the steric interference caused by the Erm methyltransferase.

Cryo-EM structure of CLC in complex with the ribosome of lincosamide-sensitive Staphylococcus aureus

To shed light on the structural basis of CLC binding to ribosome and its increased potency against A2058-dimethylated ribosomes relative to clindamycin, we first solved the cryo-EM structure of a *S. aureus* JE2 lincosamide-sensitive 70S ribosome in complex with this compound at an overall resolution of 2.98 Å (Extended Data Fig. 1C). After unsupervised 3D classification, our analysis revealed the presence of two dominant well-defined subpopulations of 70S ribosomes corresponding to (1) the non-rotated and (2) rotated 30S subunit, respectively. Since non-rotated ribosomes showed weak electron density for a tRNA in the P site, which was co-purified with the ribosome from the cell lysate, we further classified them into two subsets based on the presence or absence of P-site tRNA (Extended Data Fig. 1A). Only the class corresponding to non-rotated 70S ribosomes containing P-site tRNA, which was assigned as initiator fMet-tRNA^{fMet} (Extended Data Fig. 2A-C), was further refined and used for model building. Density corresponding to A-site tRNA could not be observed in any of the classes obtained by 3D classification, indicating that CLC interferes with the proper placement of incoming aminoacyl-tRNA, in agreement with the proposed mechanism of lincosamide action – hindering A-tRNA binding (Douthwaite, 1992; Schlünzen et al., 2001) – and with the results of the toeprinting assays (Fig. 3C,D).

The local resolution extending to 2.62 Å in the core of the particle (Extended Data Fig. 1D-F), and the well-resolved electron density corresponding to the antibiotic, enabled us to model CLC in its binding site. As expected, CLC binds in the canonical lincosamide binding pocket within the highly conserved PTC of the large ribosomal subunit (Figs. 5C and 1A-C) and extends into the nascent peptide exit tunnel (Fig. 5). The CLC binding site on the *S. aureus* ribosome overlaps accurately with the binding site of other lincosamides, e.g., clindamycin on the *E. coli* ribosome (PDB 8CGD) (Fig. 5C) or lincomycin on the *S. aureus* ribosome (PDB 5HKV). No secondary binding site of CLC has been found.

The resolution of the experimental map used for model building does not allow us to model non-covalent interactions between the antibiotic and the ribosome with high confidence. However, based on the similarity with other lincosamides bound to different ribosomes, we can expect the presence of several hydrogen bonds formed mostly between the antibiotic thiooctose core and the nucleotides A2058, A2059 and A2503 of 23S rRNA (Fig. 5B). Besides these, a CLC-specific π-stacking interaction is formed between the salicylate moiety and 23S rRNA nucleotide C2611 (Fig. 5B). We refer to this conformation of CLC as S^R (sensitive ribosome).

Of note, the less-well-defined density for the salicylate moiety and the carbon linker connecting it with the thiooctose core (Extended Data Fig. 3A) indicates partial intrinsic flexibility, which is further

supported by very weak density that could correspond to the salicylate moiety in several alternative, substantially less stable, CLC conformations (Extended Data Fig. 5A-C). Since the salicylate moiety of CLC is positioned distal to the PTC and exhibits considerable mobility, its contribution to sterically blocking A-site tRNA accommodation is inferred to be minor, a finding supported by previous biochemical experiments (Fig. 4).

Cryo-EM structure of CLC in complex with the ribosome of lincosamide-resistant Staphylococcus aureus

To determine how CLC circumvents Erm-mediated resistance, we solved the cryo-EM structure of CLC bound to A2058-dimethylated 70S ribosome at an overall resolution of 3.01 Å (Extended Data Fig. 4D). Contrary to the lincosamide-sensitive ribosomes, we observed three major subpopulations of 70S ribosome after unsupervised 3D classification, corresponding to (1) the non-rotated 30S subunit with weak tRNA density in the P-site, which was co-purified with the ribosome from the cell lysate, (2) the rotated 30S subunit, and (3) a 30S head-swivel, respectively. In addition, our analysis revealed the presence of a fourth minor subpopulation (less than 3%) of 70S ribosome corresponding to the intermediately rotated 30S subunit containing well-resolved A, P, and E-site tRNAs (Extended Data Fig. 4A). This subclass, however, seemed not to include the antibiotic bound to its canonical binding site (Extended Data Fig. 4B), and therefore, was not further processed. Despite using an antibiotic concentration significantly exceeding the inhibitory concentration (Extended Data Fig. 6A) during cryo-EM sample preparation, no secondary binding site of CLC was identified. Moreover, the presence of 70S subpopulations typical for active translation, and not containing bound antibiotic, suggests partial protection of the ribosome by A2058-dimethylation. This structural observation aligns with the *in vitro* antimicrobial testing,

which demonstrated that while CLC circumvents resistance, it remains approximately three orders of magnitude less potent against strains harbouring Erm methyltransferases than those with unmodified ribosomes (Fig. 2A). As with the lincosamide-sensitive ribosomes, we further sorted non-rotated particles into two subsets based on the presence of P-site tRNA. Only the subset of non-rotated 70S ribosomes carrying a P-site tRNA, which was assigned as initiator fMet-tRNA^{fMet} (Extended Data Fig. 2D-F), was completely refined and used for model building (Extended Data Fig. 4A).

Local resolution extending to 2.75 Å in the ribosomal core (Extended Data Fig. 4E-G) and well-resolved density corresponding to the antibiotic enabled accurate modelling of CLC in the A2058-dimethylated binding site. Notably, the density map revealed that Erm-mediated modification of this nucleotide's base induces a pronounced conformational change of CLC. Steric hindrance from the dimethyl groups displaces the thiooctose core by ~0.7 Å (Fig. 6D), disrupting the canonical interaction of the salicylate with C2611 (CLC conformation S^R). Instead, the salicylate undergoes an ~8 Å swing to establish a new π-stacking interaction with the adjacent nucleotide C2610 (Fig. 6B-D). We refer to this CLC conformation as R^R (resistant ribosome). In parallel, the dimethylated A2058 itself shifts by ~0.9 Å away from the

antibiotic relative to its position in the non-methylated ribosome–CLC complex (Fig. 6D). A comparable displacement of A2058 has been reported for other synthetic lincosamide analogues, iboxamycin (Mitcheltree et al., 2021) and cresomycin (Wu et al., 2024), although in those cases the shift is larger (~2 Å). In the CLC–ribosome complex, the smaller nucleotide displacement is compensated by the dramatic antibiotic rearrangement, particularly the shift of the thiooctose core accompanied by extensive salicylate reorientation (Fig. 6D).

Similar to the sensitive ribosomes, density corresponding to the salicylate moiety and the carbon linker in the R^R conformation is less well defined (Extended Data Fig. 3D), suggesting that the salicylate is also intrinsically flexible in this context. In addition, we observed very weak density corresponding to the S^R conformation (Extended Data Fig. 5D-F). In contrast to the lincosamide-sensitive sample, this signal is likely attributable to structural heterogeneity arising from incomplete methylation of the ribosomal pool (Extended Data Fig. 6C).

DNATCO-guided analysis reveals localized rRNA conformational effects induced by CLC

To assess CLC-induced conformational changes in 23S rRNA, we compared lincosamide-sensitive and A2058-dimethylated ribosome cryo-EM structures using DNATCO (Černý et al., 2020, 2026) (Supplementary Tables 3 and 4; a more detailed description of the analysis in Supplementary Information). DNATCO decomposes the RNA chain into overlapping dinucleotide steps and assigns each step to a nucleotide conformer class (NtC) according to its geometry, enabling sensitive and accurate detection of local three-dimensional differences. The overall NtC assignments were highly similar between the two CLC-ribosome complexes.

Within a 15 Å radius of the antibiotic, encompassing 77 dinucleotide steps, all but four steps were consistently assigned to the same NtC class in the two structures. In this area, none of the atypical, unassigned steps could be further refined to match one of the standard NtC classes (RMSD to a closest standard NtC representative <0.5 Å) (Supplementary Tables 3 and 4). Notably, the four divergent dinucleotide steps include the A2058_A2059 step, which comprises two nucleotides essential for lincosamide binding and resistance (Fig. 1B). The dimethylated mA2058_A2059 dinucleotide step in the lincosamide-resistant ribosome adopts the canonical AA09 NtC conformation, matching several previously reported drug-bound and vacant bacterial ribosome structures (Supplementary Table 5 and Supplementary Fig. 4). Surprisingly, in the lincosamide-sensitive ribosomes with CLC in S^R conformation, the same step remains unassigned and deviates markedly from canonical A-form geometries. This distortion persisted despite extensive refinement, indicating that CLC binding to the sensitive ribosome perturbs the local conformation of the A2058_A2059 dinucleotide step and induces a pronounced distortion of the A2059 ribose conformation (Fig. 6E and Supplementary Fig. 4). This effect likely arises from tension caused by the proximity of its salicylate moiety to nucleotide C2611. Notably, CLC in the R^R conformation, where salicylate interacts with more distal nucleotide C2610, restores the canonical

geometry of the mA2058_A2059 dinucleotide step regardless of the A2058 methylation (Supplementary Fig. 4). Together, these data reveal that CLC binding to sensitive ribosomes induces subtle conformational rearrangements in the 23S rRNA; these perturbations may contribute to the observed lower ribosomal affinity of CLC relative to clindamycin (Fig. 4B), thereby providing deeper structural insights into the dynamic nature of lincosamide-ribosome interactions.

MD simulations support the high mobility of the salicylate moiety observed in cryo-EM analysis

To obtain further insights into the flexibility and dynamics of CLC in its binding site, we performed atomistic molecular dynamics simulations on both lincosamide-sensitive and A2058-dimethylated *Staphylococcus aureus* ribosomes. The simulations utilized a reduced system (extending 48 Å from the CLC binding site and including the P-tRNA; Supplementary Fig. 5) derived from our experimental cryo-EM structures (see Methods for details). Three independent 100 ns replicates (Movie S1-6, Supplementary Fig. 8-13) revealed that, indeed, in both models, the salicylate moiety exhibits substantially higher flexibility compared to the propyl proline moiety (Supplementary Fig. 6C-F), the latter of which directly interferes with A-site tRNA accommodation. Moreover, the loss of interaction with the dimethylated A2058 residue led to higher mobility and lower reproducibility across the simulations for the resistant ribosome model (Supplementary Fig. 6A, B and 7A, B). In the lincosamide-sensitive model, the simulation revealed two main alternative conformations (labeled as **i** and **ii** in Fig. 6F). In contrast, the lincosamide-resistant model revealed four distinct conformations (**i**-**iv** in Fig. 6G), underscoring the increased flexibility triggered by A2058 dimethylation. Notably, the most prevalent conformations identified in the simulations (**i** for the lincosamide-sensitive and **ii** for the A2058-dimethylated model) correspond to the structures determined by cryo-EM analysis (Extended Data Fig. 5A-F). The results (Supplementary Fig. 6-11) show extensive fluctuation of CLC within the binding site, indicating sufficient geometry sampling of the conformational space with the time scale of the MD simulations. Altogether, these simulations corroborate the cryo-EM observations and highlight the high intrinsic dynamics of the salicylate moiety within the binding pocket, where it adopts two dominant conformational states depending on the presence or absence of A2058 dimethylation.

Discussion

Here, we describe CLC, a hybrid lincosamide comprising a chlorinated core functionalized with side chains derived from both celesticetin and lincomycin. While the antibacterial spectrum of CLC mirrors that of traditional lincosamides targeting Gram-positive pathogens, it exhibits increased potency relative to clindamycin. This enhanced efficacy is particularly pronounced against clinical isolates harboring lincosamide-resistance determinants, including ribosomal protection proteins and 23S rRNA methyltransferases. Notably, the robust activity of CLC against *Clostridioides difficile*—a pathogen intrinsically resistant to clindamycin—suggests clinical potential. By maintaining direct activity against *C.*

difficile, CLC may mitigate the risk of development of *C. difficile*-associated diarrhea typically associated with lincosamide therapy.

We demonstrate that the superior potency of CLC is driven primarily by enhanced intracellular accumulation, which facilitates ribosomal engagement across both lincosamide-sensitive and resistant strains (Fig. 4C). This accumulation advantage likely stems from increased membrane permeability rather than evasion of specific efflux systems. Notably, CLC maintains a consistently high relative potency across a diverse spectrum of Gram-positive bacteria, regardless of the multidrug transporters they employ (Schindler and Kaatz, 2016). Furthermore, CLC exhibited markedly improved activity against *Escherichia coli* lacking the TolC multidrug exporter compared to clindamycin. This finding suggests that structural modifications in CLC also enhance penetration through the Gram-negative outer membrane, effectively broadening the potential utility of the lincosamide scaffold.

A comparative analysis of lincomycin, clindamycin, ODC, and CLC elucidates how discrete chemical modifications cumulatively enhance antibacterial potency. While C7-chlorination or salicylate attachment independently augment cellular uptake, as evidenced by the transitions from lincomycin to clindamycin and ODC, respectively, their convergence in the CLC scaffold exerts a synergistic effect on intracellular accumulation. Notably, these findings resolve a longstanding ambiguity regarding the mechanistic basis for clindamycin's superior performance over its parent compound, lincomycin, by demonstrating that C7-chlorination is a primary driver of enhanced intracellular accumulation (Matzov et al., 2017).

Although CLC does not fully overcome resistance in A2058-dimethylated strains, its sustained affinity highlights a viable path for future scaffold optimization. We demonstrate that CLC utilizes unique molecular interactions, distinct from those of iboxamycin and cresomycin, to maintain efficacy against modified ribosomes, expanding the chemical space available for overcoming Erm-methylation. In the case of iboxamycin, increased activity is conferred by a rigid, bicyclic oxepanoprolinamide scaffold that maximizes steric overlap with the A- and P-site tRNA binding regions (Mitcheltree et al., 2021). Cresomycin further augments ribosomal affinity of iboxamycin by pre-organizing the lincosamide moiety into its ribosome-bound conformation (Wu et al., 2024). Crucially, both iboxamycin and cresomycin overcome resistance by inducing a 2Å displacement of the dimethylated A2058 nucleotide. A comparable strategy for overcoming Erm-mediated resistance has been observed with macrolones, a novel class of hybrid antibiotics that combine a macrolide core with a quinolone moiety. In these compounds, the fluoroquinolone moiety establishes unique interactions with the ribosome, increasing the binding affinity sufficiently to counteract the detrimental effects of A2058 dimethylation by displacing the modified residue from its canonical position (Aleksandrova et al., 2024).

In contrast, our cryo-EM analysis reveals that CLC employs a slightly different mechanism. Rather than forcing a rigid-body displacement, CLC leverages remarkable conformational flexibility to accommodate the modification. This enables a coordinated shift of the thiooctose core, paired with a partial displacement of the dimethylated nucleotide and a reorientation of the salicylate moiety. This rearrangement allows the salicylate to engage in a compensatory stacking interaction with an alternative

nucleotide within the nascent peptide exit tunnel (NPET), effectively offsetting the loss of the two hydrogen bonds typically disrupted by A2058 methylation. However, this inherent flexibility (Fig. 6, Extended Data Fig. 5) limits binding affinity in sensitive ribosomes relative to clindamycin (Fig. 4B). This observation highlights a clear trade-off between conformational plasticity and the stability of target engagement. Consequently, future design efforts aimed at pre-organizing the salicylate-nucleotide interactions within the NPET may enhance binding affinity, potentially yielding superior potency across both susceptible and resistant pathogens.

Figure preparation

The graphical abstract was created with BioRender.com (Novotná, M. (2026) https://BioRender.com/co2xux3). The structures of all compounds were prepared in ACD/ChemSketch v2023 or ChemDraw v.23.0.1.10. Plots were produced with LibreOffice v.24.2.7.2, GraphPad v.10, or R v.4.3.2. Figures showing cryo-EM densities or atomic models were prepared using UCSF ChimeraX v.1.7, v.1.8, v.1.9, or v.1.10 (Meng et al., 2023). Figures showing structures from MD simulations were prepared using VMD v2.0.0a7. Final figures were assembled in Inkscape v.1.4.2.

Methods

Bacterial strains

For Antibiotic susceptibility testing, standard reference strains from the American Type Culture Collection (ATCC; Manassas, VA, USA) were used in addition to a panel of clinical and commensal isolates with characterized resistance phenotypes and, in many cases, also genotypes. Details on these isolates, including their source and resistance mechanisms, are provided in Supplementary Fig. 2.

For functional and structural characterization of compounds, the laboratory strain *Staphylococcus aureus* RN4220 and *S. aureus* JE2, a methicillin-resistant USA300 derivative strain originally isolated from a skin and soft tissue infection in Los Angeles County, California, along with JE2 transposon mutants NE1858 and NE854 (JE2::*ermB*$_C$) (Fey et al., 2013) harboring constitutively expressed *ermB* inserted into the ABC transporter ATP-binding protein StpC or the lantibiotic ABC transporter ATP-binding protein, respectively, were obtained from BEI Resources (Supplementary Table 7).

Celesticetin purification

Streptomyces caelestis ATCC 15084 was cultivated for celesticetin production. A seed culture was prepared by inoculating spores into 50 ml of YEME medium in 500 ml flat-bottom boiling flasks and incubated at 28°C with shaking at 180 rpm for 30 h. A 2.5 ml aliquot of this culture was then transferred to 47.5 ml of AVM (Najmanová et al., 2014) medium in 500 ml baffled flasks and cultivated under identical conditions for 120 h. Supernatants from ten such flasks were pooled for further processing.

Cells were removed by centrifugation at 4,000 × g for 10 min at 4°C. The resulting supernatant was acidified to pH 3 with formic acid and stored at − 20°C until extraction. For solid-phase extraction, Amberlite XAD-4 resin was packed into a glass column (5 cm diameter × 10 cm height). The column was equilibrated with 400 ml of methanol, followed by 400 ml of 0.05% (v/v) aqueous formic acid, before loading 300 ml of the acidified supernatant. The column was washed with 400 ml of 0.05% aqueous formic acid, and bound compounds were eluted with increasing concentrations of methanol in 0.05% aqueous formic acid. Fractions of 400 ml were collected at each methanol concentration, except for the 50% methanol step, where 5.2 liters were collected. Celesticetin was found in the 50% methanol eluate, which was pooled and evaporated to dryness using a parallel rotary evaporator (SyncorePlus, Büchi, Switzerland). Further purification was performed by a two-step preparative high-performance liquid chromatography (HPLC; LC-20AP, Shimadzu, Japan). The first step utilized a Triart Prep C18-S column (250 × 20 mm, 10 µm; YMC, Japan) with a binary mobile phase consisting of 0.1% formic acid (A) and acetonitrile (B), delivered at 14 ml/min using the following linear gradient: 0 min at 5% B, 5 min at 5% B, 40 min at 100% B, followed by a 10 min column wash at 100% B and a 10 min re-equilibration at 5% B. The second HPLC step used an XTerra Prep RP18 column (150 × 7.8 mm, 5 µm; Waters, USA) with an isocratic elution of 0.1% formic acid:acetonitrile (75:25, v/v). Fractions containing celesticetin were identified offline using an Acquity UPLC system equipped with a 2996 photodiode array detector (PDA) and an LCT Premier XE time-of-flight high-resolution mass spectrometer (Waters, USA). For analysis, 5 µL of the sample was injected onto an ACQUITY PREMIER CSH C18 column (2.1 × 50 mm, 1.7 µm) maintained at 40°C. Separation was achieved with a binary mobile phase consisting of 0.1% formic acid (A) and acetonitrile (B), delivered at 0.4 ml/min using the following linear gradient: 0 min at 5% B, 1.5 min at 5% B, 6 min at 27% B, followed by a 1 min column wash at 100% B and a 2 min re-equilibration at 5% B. Mass spectrometry was performed in positive ionization mode with the following settings: capillary voltage + 2,800 V, cone voltage + 40 V, source temperature 120°C, desolvation temperature 350°C, desolvation gas flow 650 l/h, cone gas flow 50 l/h. Leucine-enkephalin (2 ng/µL, 5 µl/min) was used as a lock mass for accurate mass calibration. Data were processed using MassLynx v4.1 software, and celesticetin was identified by extracting the $[M + H]^+$ ion at 529.22 with a tolerance of ± 0.05 Da and inspecting the MS spectra. Quantification was performed using diode array detection at 305 nm, the absorption maximum of celesticetin, with OD-Celin (for synthesis see the respective Results and Methods part) used as a standard due to its identical absorbance properties. The yield of celesticetin from 300 ml of culture broth supernatant was 1.1 mg at > 95% purity (monitored at 220 and 305 nm).

Single-crystal X-ray crystallography

M = 1313.24 g.mol^{-1}, orthorhombic system, space group $P2_12_12_1$, a = 11.7535 (2) Å, b = 14.6505 (4) Å, c = 37.6933 (6) Å, Z = 4, V = 6490.6 (2) Å^3, D_c = 1.344 g.cm^{-3}, μ(Cu-$K\alpha$) = 2.88 mm^{-1}, crystal dimensions of 0.43 × 0.06 × 0.04 mm. Data were collected at 180 (2) K on a Supernova diffractometer equipped with an Atlas S2 CCD detector with a microfocus sealed tube Cu-$K\alpha$ radiation. The data reduction, scaling, and absorption correction were handled in CrysAlisPRO (Rigaku Oxford Diffraction, 2017). The structure was

solved by charge flipping methods (Palatinus and Chapuis, 2007) and anisotropically refined by full matrix least squares on *F* squared using the CRYSTALS (Betteridge et al., 2003) to final value $R = 0.050$ and $wR = 0.128$ using 12491 independent reflections ($\theta_{max} = 72.8°$), 837 parameters and 56 restrains. The hydrogen atoms bonded to carbon atoms were placed in calculated positions refined with riding constraints, while the hydrogen atoms bonded to oxygen and nitrogen atoms were located in residual electron density maps and refined with restrained geometry. The electron density maps were visualized using MCE (Rohlíček and Hušák, 2007). For further information on data collection and refinement, see Supplementary Table 1. The structure model was visualized using Diamond 3.0 (Brandenburg and Putz, 1999). The structure was deposited into the Cambridge Structural Database under accession number CCDC 2529822.

Antibiotic susceptibility testing

Antimicrobial susceptibility testing of *C. difficile* strains was performed by the agar microdilution method in 200 µl of Wilkins-Chalgren anaerobe agar (MH, Oxoid) dispensed into 48-well flat-bottom plates (JetBiofil). The plates were incubated anaerobically at 37°C for 24 hours. Antibiotic susceptibility testing of other bacterial strains was performed by the broth microdilution method according to ISO standard 20776-1 in 100 µl Mueller-Hinton broth (MH, Oxoid) in a 96-well flat-bottom plate (Thermo Fisher Scientific). Antibiotics were dissolved in DMSO and diluted by serial two-fold dilution. Wells were inoculated with 5 µl of the cell suspension in 0.9% NaCl (McF 0.5-1). Parafilm was used to eliminate evaporation, and the plates were incubated for 16 hours at 37°C. End-point absorbance at 600 nm was measured on a BioTek Synergy HT microplate reader. The minimal concentration of the compound required to inhibit visible bacterial growth was assessed as the MIC. All measurements were performed in duplicates three times, at a minimum.

Total RNA isolation

12 ml of Brain Heart Infusion (BHI, Oxoid) media was inoculated with 600 µl of *Staphylococcus aureus* JE2 cell suspension (in 0.9% sodium chloride solution, McF 1) and *Staphylococcus aureus* NE1858 (JE2::$ermB_C$), respectively. Subsequently, 12 ml of BHI media was supplemented with erythromycin (final concentration 50 µg/ml) and inoculated with *Staphylococcus aureus* NE1858 (JE2::$ermB_C$). Bacteria were grown at 37°C (200 RPM). After reaching an optical density of 1 at 600 nm, cells were collected, and the pellet was stored at − 80°C. The pellet was resuspended in 250 µl of TE buffer (10 mM Tris-HCl, 0.1 mM EDTA, pH 8), and cells were disrupted on FastPrep (60 sec, 6 movements/sec) using Lysing Matrix B. Immediately, 750 µl of TRIzol™ Reagent (Ambion) was added, and the sample was incubated for 5 min at room temperature. After the addition of 200 µl of chloroform and system equilibration, the sample was centrifuged, and the water phase was separated and mixed with 500 µl of isopropanol for precipitation. After the precipitated total RNA was dissolved in water and treated with DNase I (NEB), the total RNA was purified using the Ribospin™ vRD (GeneAll) kit and stored as a water solution for a short

period at − 20°C. The integrity was analyzed on a 2% agarose gel, and the quantity was measured on the Nanodrop (DeNovix).

Primer extension inhibition assay

The protocol was adapted from the study of Bailey and colleagues (Bailey et al., 2008) with the following modifications. The A2058-methylation status in *Staphylococcus aureus* was detected with the primer *A2058met_Sa_YY* labeled at the 5' end with the fluorescent dye Yakima Yellow (Supplementary Table 9). For better efficiency, we used 0.1 µl of undiluted avian myeloblastosis virus reverse transcriptase at a concentration of 10,000 units/ml (Promega) in the extension reaction premix per reaction sample. The cDNA pellet was dissolved in 3 µl of formamide loading dye (95% formamide, 20 µM EDTA, pH 8, 0.00025% bromphenol blue), denatured at 95°C for 5 min and analyzed on a 12% sequencing polyacrylamide gel (42 cm height, 20 cm width, 0.4 mm depth) in TBE buffer (10.8% Trizma Base, 5.5% boric acid, 20 mM EDTA, pH 8). The gel was run for 2.5 hours at 40 W and imaged on Typhoon™ FLA 9500 (GE Healthcare Life Sciences). The quantification was calculated in ImageJ v1.53e (Source Data).

Ribosome purification

Lincosamide-sensitive and lincosamide-resistant 70S ribosomes were prepared from *Staphylococcus aureus* JE2 and *Staphylococcus aureus* NE1858 (JE2::*ermB*$_c$), respectively. 1 liter of Brain Heart Infusion (BHI, Oxoid) media supplemented optionally with 1% glycine was inoculated with 3 ml of overnight cell culture, and bacteria were grown at 37°C (200 RPM). After reaching optical density 1 at 600 nm, cells were collected, and the pellet was stored at − 80°C. The pellet was resuspended in 8 ml of ice-cold buffer A (20 mM Tris-HCl, pH 7.5, 10.5 mM $MgCl_2$, 100 mM NH_4Cl, 0.5 mM EDTA, pH 8) supplemented with SIGMA*FAST*™ Protease Inhibitor (Sigma-Aldrich) and the cells were disintegrated using CryoMill (Retsch) (initial cooling 8 min – speed 5 s^{-1}, 5 x 3 min cycles: speed 30 s^{-1}, intermediate cooling 1 min – speed 5 s^{-1}). The defrosted cell lysate was centrifuged, and the supernatant was further clarified by filtration (0.45 µm). The sample was layered on a 37.7% sucrose cushion in buffer B (20 mM Tris-HCl, pH 7.5, 15 mM $MgCl_2$, 500 mM NH_4Cl, 0.5 mM EDTA, pH 8) and ultracentrifuged overnight. The ribosomal pellet was washed with 5 ml of ice-cold buffer A supplemented with SIGMA*FAST*™ Protease Inhibitor (Sigma-Aldrich), centrifuged, and 5 ml of the supernatant was mixed with another 5 ml of buffer A and 10 ml of buffer B. The total concentration of NH_4Cl was adjusted to a final concentration of 500 mM by the slow addition of 2 ml 4M stock solution. The ribosomes were pelleted by ultracentrifugation for 2 h, and the ribosomal pellet was resuspended in 500 µl of Storage buffer (20 mM Tris-HCl, pH 7.5, 10 mM $MgCl_2$, 50 mM NH_4Cl, 0.1 mM EDTA, pH 8, 6 mM β-mercaptoethanol) and stored at − 80°C. To evaluate the quality of purification, 20 µl of 20 U/µl ribosomes were analyzed on a 10–40% sucrose gradient (in storage buffer). After ultracentrifugation for 2.5 h at 39,000 RPM, the profile was analyzed on Gradient Station (BioComp) or Brandel BR-188 Density Gradient Fractionation System with a UA-6 Teledyne ISCO detector

and a Foxy Jr.® Fraction Collector. The absorbance profile of the sample was measured continuously at 254 nm.

Preparation of staphylococcal 30S extract and in vitro translation inhibition assay

A cell-free extract was prepared from *Staphylococcus aureus* RN4220 as described in (Kwon and Jewett, 2015; Silverman et al., 2019) with minor modifications. 1 liter of TSB was inoculated with an overnight cell culture to an initial OD_{600} = 0.01, and grown at 37°C, 220 rpm until the culture reached mid-log phase (OD_{600} ~3–4). The culture was chilled on ice for 30 min, then centrifuged (8,000 rpm, 10 min, 4°C). The pellet was washed twice with 50 ml Buffer A1 (10 mM Tris-acetate pH 8.0, 14 mM Mg-acetate, 1 M KCl, 1 mM DTT), then once with 25 ml Buffer A2 (10 mM Tris-acetate pH 8.0, 14 mM Mg-acetate, 50mM KCl, 1 mM DTT) and stored at − 80°C. For lysis, the pellet was resuspended in Buffer B (10 mM Tris-acetate pH 8.0, 20 mM Mg-acetate, 50 mM KCl, 2 mM DTT, 1× protease inhibitor) at 0.7 ml per gram of pellet. The bacterial suspension was transferred to FastPrep tubes (800 µl in 2ml tubes with 0.7 g of 0.1 mm glass beads) and lysed in 5 cycles (speed 6, 40 sec). After a 10-minute ice incubation, debris was pelleted (13,000 rpm, 10 min, 4°C). The supernatant was clarified by two centrifugations (21,000 × g, 15 min, 4°C), aliquoted, flash-frozen in liquid nitrogen, and stored at − 80°C for TX-TL analysis.

The translation inhibition assay was performed using an *in vitro* coupled transcription/translation system adapted from *E. coli* S30 Extract System for Circular DNA (Promega) with an in-house prepared *S. aureus* S30 extract. Each assay was conducted in a final volume of 15 µl, containing 4.5 µl of *S. aureus* RN4220 cell extract, 6 µl of "S30 Premix without Amino Acids" (Promega, ref L512A), 1.5 µl of "Amino Acid Mixture, Complete (1 mM)" (Promega, ref L4461), and 1 µg of pRN12 plasmid (Addgene plasmid #84456) (De Jong et al., 2017) (Supplementary Table 8) encoding the fluorescent protein mAmetrine under the control of the strong constitutive *S. aureus* promoter PsarA. Negative controls lacked the DNA template. Reactions were incubated at 30°C, and mAmetrine fluorescence was measured every 15 minutes (λ_{ex}: 423 nm / λ_{em}: 525 nm) using a TECAN Infinite 200Pro reader. For inhibition assays, 2 µl of a 7.5× concentrated antibiotic solution (or water for controls) was added to 13 µl of the reaction mix. Each inhibition reaction was performed in triplicate, with four independent biological replicates using two different batches of cell-free extract. Data was analyzed and visualized using GraphPad Prism v10 software.

Competitive displacement assay

Ribosome-antibiotic stock solution was prepared with 250 nM *S. aureus* JE2 ribosomes and 250 nM lincomycin in a binding buffer composed of 20 mM Tris-HCl (pH 7.5), 10 mM $MgCl_2$, 150 mM NH_4Cl, and 6 mM β-mercaptoethanol. This mixture was incubated at 37°C for 10 minutes. For the assay, 100 µl aliquots of the ribosome-antibiotic complex were dispensed into 1.5 ml tubes. To immobilize the

complex, 10 µl of DEAE magnetic beads were added to each tube. The beads were pre-washed once with H_2O (100 µl) and twice with the binding buffer (100 µl each). The suspensions containing the beads and complexes were incubated at 23°C for 10 minutes. After the incubation, the beads were captured magnetically, the supernatant was discarded, and the beads were washed with 100 µl of ice-cold binding buffer to eliminate any unbound lincomycin. The displacement assay was initiated by adding 100 µl of clindamycin or CLC solution, varying in concentration from 1 nM to 100 µM, while maintaining a constant final DMSO concentration of 0.1%. The reactions were incubated for 1 hour at 37°C. Following magnetic capture of ribosomes, the final eluent (supernatant) containing the displaced lincomycin was collected and transferred to new tubes for quantification via LC-MS. The assay was performed in technical duplicates with two independent biological repetitions

Intracellular accumulation assay

The intracellular accumulation of antibiotics was quantified using the silicone oil centrifugation method followed by LC-MS analysis (*E. coli* protocol: (Iyer et al., 2018)) with slight modifications. The *S. aureus* strains JE2 and its derivative JE2::$ermB_C$ (NE854) were cultured overnight in BHI (supplemented with 5 µg/ml erythromycin for NE854), diluted 1:500 into prewarmed TSB, and grown to OD600 = 0.55–0.60. Cells (200 ml) were pelleted (2,465 g, 4°C), washed once in 60 ml PBS, and resuspended in 8.8 ml PBS and aliquoted (875 µl each). One aliquot was used for colony-forming unit (CFU) determination by serial dilution of the suspension, with 10^{-7} and 10^{-8} dilutions plated (500 µl). The final CFUs were determined by a calibration curve. Aliquots were equilibrated at 37°C for 10 min before adding the antibiotic stock (5 mM in DMSO, 8.75 µl) to reach a final concentration of 50 µM and incubating for 10 min at 37°C. Samples (800 µl) were immediately layered onto precooled silicone oil (9:1 AR20/ High-temperature silicone oils (Millipore Sigma), -78°C) and centrifuged (13,000 g, 2 min, RT) to pellet the cells. Following precise removal of the medium and oil layers via vacuum aspiration and P100 pipetting, cell pellets were resuspended in 300 µL of 40:40:20 acetonitrile:methanol:water (LC-MS grade) and lysed by bead beating (0.45 g, 0.1 mm zirconium beads, Speed 6, 40s, 3x with cooling on ice). Lysates were cleared by three rounds of centrifugation (1,000 rpm, 30s; 13,000 g, 2 min, RT; and 20,000 g, 10 min, RT), and the final supernatant (150 µl) was collected for LC-MS analysis. The experiment was repeated twice with three independent biological replicates.

LC-MS and antibiotic quantification

Samples were analyzed using an Agilent 1290 Infinity II UHPLC system (Agilent Technologies, Waldbronn, Germany) coupled to a timsTOF HT mass spectrometer (Bruker Daltonics, Bremen, Germany). The instrument was operated in positive electrospray ionization (ESI+) mode under data-dependent acquisition (DDA) using the PASEF (Parallel Accumulation–Serial Fragmentation) workflow.

Chromatographic separation was performed on a Waters ACQUITY Premier CSH C18 column (1.7 µm, 2.1 × 100 mm) maintained at 40°C. Mobile phase A consisted of ultrapure water with 0.1% formic acid (100:0.1, v/v), and mobile phase B consisted of acetonitrile. The flow rate was set to 0.4 ml/min with the following gradient: 5% B for 1.5 min, 5–46% B in 8.5 min, 46–100% B in 5 min, 100% B for 2 min, 100-5% B in 2 min, and re-equilibrated at 5% B for 3 min.

The multisampler temperature was maintained at 4°C throughout the analysis. Carry-over was minimized by enabling the multi-wash function, performing external needle washing and seat backflushing with water, 50% methanol, and methanol for 15s each prior to every injection.

Data was processed and quantified using TASQ software (version 2025b, Bruker Daltonics). Prior to integration, mass recalibration was performed for each analytical batch using sodium formate cluster ions to ensure high mass accuracy. Quantification was carried out in a targeted manner based on extracted ion chromatograms of the corresponding precursor ions, and peak areas were normalized against the internal standard pirlimycin to correct for potential variability in ionization efficiency and injection volume.

Chromatographic peaks were smoothed using a Savitzky–Golay algorithm, and only signals exceeding a signal-to-noise threshold of 500 ion counts were considered for further analysis. Feature alignment across samples was performed using a mass tolerance of 5 ppm and a retention time tolerance of 0.3 min. Background signals detected in solvent blanks were subtracted from all samples prior to quantification.

External calibration curves were generated individually for each antibiotic using a linear regression model weighted by $1/x^2$ across specific concentration ranges for each antibiotic. For chloramphenicol, clindamycin, and ODC, the linear range was 19.5312 – 0.3051µM, for CLC was 0.6103 – 0.0047µM and for lincomycin was 1.2207 – 0.0190 µM. Linearity of each calibration curve was evaluated with a coefficient of determination (R^2) of 0.99849 for chloramphenicol, 0.99528 for CLC, 0.98958 for clindamycin, 0.98280 for lincomycin, and 0.99448 for ODC. All antibiotics were quantified using compound-specific calibration curves, with the same internal standard (pirlimycin) applied across all analytes.

Toeprinting assay

Toeprinting was performed as described previously (Orelle et al., 2013). Briefly, commercially-acquired DNA templates (full sequences provided in Supplementary Table 10) containing a T7 promoter, ribosome binding site, *ermBL* variant sequence coding for the MLVFQMRNVDKTSTILKSE peptide (*TP_ermBLv*) (Seip et al., 2018) or *ermDL* variant sequence coding for the MTHSMRLRFPTLNQISE peptide (*TP_ermDLvIle*), respectively, and the NV1 sequence were amplified by PCR using the primers *FP_T7_TP* and *RP_NV1_TP* (Supplementary Table 9). DNA templates were transcribed *in vitro* using T7 RNA Polymerase (New England Biolabs) and NTPs (Thermo Fisher Scientific) according to the manufacturer's

instructions and then purified using the RNA Clean & Concentrator Kit (Zymo Research). Mupirocin dissolved in DMSO, and either pure DMSO or lincosamide antibiotics dissolved in DMSO were evaporated in 1.5 ml tubes prior to the addition of the translation reaction mixture. Mupirocin inhibits isoleucyl-tRNA synthetase and thus induces ribosome stalling when an Ile codon is in the A-site. mRNA template at a final concentration of 1 µM or 2 µM, respectively, was translated *in vitro* in a 5 µl reaction volume in the presence of mupirocin at a final concentration of 50 µM and lincosamide antibiotic at an indicated final concentration using PURExpress Δ Ribosome Kit (New England Biolabs) and ribosomes purified from *Staphylococcus aureus* JE2 or NE1858, respectively, at a final concentration of 2.4 µM. After incubating for 20 min at 37°C, 1 µl of Yakima Yellow-5'-labeled probe *NV_YY* (2 µM) (Supplementary Table 9) complementary to the NV1 sequence was added to the reaction, and the sample was incubated for another 5 min at 37°C. Reverse transcription was then performed with 5 U of Avian Myeloblastosis Virus reverse transcriptase (Promega Corporation) mixed with 0.4 µl of Pure System Buffer (9 mM Magnesium acetate, 5 mM Potassium phosphate, 95 mM Potassium glutamate, 5 mM NH_4Cl, 0.5 mM $CaCl_2$, 1 mM spermidine, 8 mM putrescine, 1 mM DTT) and 0.1 µl of dNTP mix (Thermo Fisher Scientific; each 10 mM) for 20 min at 37°C. RNA was degraded by adding 0.5 µl of a 10 M NaOH stock at 37°C for 15 min. Samples were neutralized with 0.7 µl of a 7.5 M HCl stock, and 20 µl of Toeprinting Resuspension Buffer was added (0.3 M Sodium acetate, pH 5.5, 5 mM EDTA, pH 8, 0.5% SDS). cDNA was purified using a Nucleotide Removal Kit (QIAGEN) and eluted with 50 µl of water. After evaporation, fully dried samples were resuspended in 3 µl of formamide loading dye (95% formamide, 20 µM EDTA, pH 8, 0.00025% Bromphenol blue).

Sanger sequencing reactions were performed with 1 pmol of DNA template treated with ExoSAP-IT reagent (Thermo Fisher Scientific) using Hemo KlenTaq polymerase (New England Biolabs), $MgCl_2$ at a final concentration of 0.6 mM, and Yakima Yellow-5'-labeled probe NV_YY at a final concentration of 0.12 µM added to a tube containing 20 µM dNTP mix and one of the ddNTP (30 µM ddGTP, 350 µM ddATP, 600 µM ddTTP, 200 µM ddCTP, respectively). The following thermocycler program was used: 60 s of initial denaturation at 95°C; 40 cycles of 30 s of denaturation at 95°C, 30 s of annealing at 42°C, and 60 s of elongation at 70°C; and an additional 5 min of elongation at 70°C. Sequencing reactions were purified by precipitation with 2% lithium chloride in acetone and resuspended in 3 µl of formamide loading dye.

Samples were analyzed by polyacrylamide gel electrophoresis, as follows. Sequencing reactions were denatured at 75°C for 3 min, the toeprinting samples were denatured at 95°C for 5 min, and both were loaded on a 6% sequencing polyacrylamide gel (42 cm height × 20 cm width × 0.4 mm depth) in TBE buffer (10.8% Trizma Base, 5.5% boric acid, 20 mM EDTA, pH 8). The gel was run for 2.5 hours at 40 W and imaged on a Typhoon™ FLA 9500 (GE Healthcare Life Sciences).

Preparation of the S. aureus 70S ribosome in complex with CLC for cryo-EM

CLC dissolved in DMSO was dried in a tube using SpeedVac and dissolved in ribosome storage buffer (20 mM Tris-HCl, pH 7.5, 10 mM $MgCl_2$, 50 mM NH_4Cl, 0.1 mM EDTA, pH 8, 6 mM β-mercaptoethanol) containing staphylococcal ribosomes at a final concentration of 0.2 μM. A final concentration of 10 μM of CLC was used for sensitive *S. aureus* JE2 ribosomes, and a final concentration of 750 μM of CLC was used for resistant *S. aureus* JE2::*ermB*$_C$ ribosomes. Following the 10-minute incubation at 37°C and short incubation on ice, 4 μl of the sample was applied to a Quantifoil (QF-R2/2-Cu 300) carbon grid, which was coated with a 2-nm carbon layer using a CCU-010 Compact Coating Unit (Safematic) and glow-discharged for 20 s at 2.5 mA using ELMO Glow Discharge System (Cordouan Technologies). Grids were plunge-frozen in liquid ethane using a Vitrobot (FEI) set to 4°C and 100% humidity with 2.5 s blotting time, blot force 5, and 30 s waiting time.

Cryo-EM data acquisition

Grids were imaged using a Talos Arctica microscope (FEI) operated at 200 kV and equipped with a K2 Summit direct electron detector (Gatan) in nanoprobe mode at the Institut Européen de Chimie et Biologie in Bordeaux (France). Images were recorded with SerialEM in counting mode with a magnified pixel size of 0.93 Å at a magnification of 45,000x. Each movie contained 38 frames with a dose per frame of 1.3 e/Å^2. For the lincosamide-sensitive ribosome complex, the final dataset was composed of 4,008 micrographs with defocus values ranging from − 0.4 to − 1.8 μm. For the lincosamide-resistant ribosome complex, the final dataset was composed of 7,236 micrographs with defocus values ranging from − 0.4 to − 1.8 μm.

Cryo-EM image processing

Data were processed in Relion v.4.0 (Kimanius et al., 2021) as shown in Extended Data Fig. 1 and Extended Data Fig. 4. Briefly, the raw movie frames were summed and corrected for drift and beam-induced motion at the micrograph level using MotionCor2 (Zheng et al., 2017). The resolution range of each micrograph and the contrast transfer function (CTF) were estimated with CTFFIND v.4.1 (Rohou and Grigorieff, 2015). Well-defined two-dimensional classes were selected by three subsequent rounds of two-dimensional classification of the particles obtained by automated picking in Relion v.4.0 (Kimanius et al., 2021). Three-dimensional classification was performed in two steps: (1) unsupervised classification with particles downsized four times; and (2) focused classification with background subtraction using a mask covering the P-site tRNA on particles downsized twice. Classes with P-site tRNA were selected for automated three-dimensional reconstruction and CTF refinement in Relion v.4.0 (Kimanius et al., 2021), followed by Bayesian polishing. The final reconstruction was sharpened by applying a negative sharpening B-factor of − 10 in Relion v.4.0 (Kimanius et al., 2021). The resolution for the electron density map was estimated in CryoSparc (Punjani et al., 2017) using the gold standard criterion (FSC = 0.143), resulting in a final reconstruction with a nominal resolution of 3 Å for both the samples, lincosamide-sensitive and lincosamide-resistant ribosome, respectively. Local-resolution

estimation was performed using Phenix v.1.20.1–4487 (Liebschner et al., 2019). The pixel size of the final electron density map was optimized by calculating model-to-map correlation coefficients at multiple pixel sizes in Chimera v.1.16 (Pettersen et al., 2004) and selecting the pixel size that yielded the highest correlation.

Atomic model building and refinement

For the lincosamide-sensitive ribosome complex, a 70S ribosome of *Staphylococcus aureus* NCTC 8325 in complex with P-site fMet-tRNA and mRNA (PDB 7NHM) was used as an initial model. Sequence adjustments and other minor alterations of the model were performed in Phenix v.1.20.1–4487 (Liebschner et al., 2019), Coot v.0.9.8.1 (Emsley et al., 2010), and ChimeraX v.1.7 (Meng et al., 2023). The initial model was rigid-body fitted into the experimental electron density map using ChimeraX v.1.7 (Meng et al., 2023) and subjected to iterative cycles of manual building and refinement in ISOLDE v.1.7 (Croll, 2018) and Coot v.0.9.8.1 (Emsley et al., 2010) followed by a concluding subtle round of real-space refinement in Phenix v.1.20.1–4487 (Liebschner et al., 2019) using the anisotropic sharpened map obtained with Phenix v.1.20.1–4487 (Liebschner et al., 2019). For the lincosamide-resistant ribosome complex, the lincosamide-sensitive ribosome complex was used as an initial model. Methylation of the A2058 nucleotide was introduced using ChimeraX v.1.7 (Meng et al., 2023). In both cases, as an initial model for the antibiotic, the model of OD-Celin docked with QSite (Schrödinger) into a sensitive or A2058-dimethylated staphylococcal ribosome model, respectively, was used, and modified using ChimeraX v.1.7 (Meng et al., 2023). Models were validated with MolProbity within the Phenix v.1.21.2–5419 (Liebschner et al., 2019), and the resulting values are reported in Supplementary Table 2. The rRNA structure, with the main focus on the region within 15 Å from the antibiotic, was analyzed and validated with the tools provided by the DNATCO web server v.5 (Černý et al., 2026) using a set of NtC classes v.3.5 (Černý et al., 2020) (Supplementary Tables 3 and 4).

MD simulations

The MD simulations were carried out using GROMACS 2020(Berendsen et al., 1995; Lindahl et al., 2001; Van Der Spoel et al., 2005) with the AMBER99SB force field. The chosen force filed is adequate for atomistic MD simulation of the ribosome (Šponer et al., 2014). The standard force field parameters were used for most of the protein and RNA residues. The specific residue formyl methionine incorporated in the 3’-end of P-site tRNA was parameterized using a standard procedure(Wang et al., 2004) with RESP charges (Bayly et al., 1993), where the total charge of the residue was constrained to 0.3081 (the charge for 3’-terminal RNA residues in AMBER99SB forcefield). The other specific RNA residue, dimethylated adenosine phosphate A2058 incorporated in the middle of the RNA chain of the ribosome of lincosamide-resistant *Staphylococcus aureus* was also parameterized using a standard procedure(Wang et al., 2004) with RESP charges(Bayly et al., 1993) (total charge of the residue was constrained to -1, standard for the middle RNA residue). The ligand CLC was parameterized using the standard

Antechamber procedure(Wang et al., 2004) with RESP charges(Bayly et al., 1993) and General AMBER Force Field. As the full 70S ribosome is extremely large, a smaller model of the 70S ribosome was introduced to enable sufficiently long MD simulations. The smaller model was constructed from our cryo-EM structures of the 70S ribosome of both lincosamide-sensitive (PDB 9I88) and lincosamide-resistant (PDB 9I89) *Staphylococcus aureus* with CLC (Supplementary Fig. 5). All residues within 48 Å of CLC were incorporated into the model. Unfortunately, this approach means that the main chains of both RNA and proteins are cut at many sites, leading to many unconnected fragments. To limit fragmentation, parts shorter than 3 residues (but with a distance greater than 45 Å from CLC) were also removed. Furthermore, if the topological distance between two fragments was smaller than 10 residues, then those residues (that would be removed from the model) were added back to the model to keep the two fragments together. The residues at the artificial cuts were converted to the terminal residues (either 5' or 3'). Since this modification leads to many 'unsupported' residues and RNA loops (that would freely move during MD simulations), which would otherwise have interactions with their neighbors in the complete 70S ribosome, the artificial position restraints (100 kJ/mol/nm^2) were introduced at the phosphate atoms of those 'unsupported' RNA residues on the surface of our model (Supplementary Table 6) during the MD simulations to keep the whole model of ribosome compact. MD simulations were performed at 310 K with the cubic box of approximate dimensions 15.3x15.3x15.3 nm. The simulation box with our model system was filled with 107,732 water molecules based on the TIP3P model and 685 Na^+ counter ions neutralizing the negative charges of RNA phosphate groups. The periodic boundary condition was applied for the simulation box. The time step was 2 fs, and the LINCS algorithm for bond constraints was applied. In order to minimize dependence of the MD simulation on the initial configuration, three statistical repeats of 100 ns of MD simulations for both lincosamide-sensitive and lincosamide-resistant 70S ribosomes (starting from the same initial geometries with different randomly generated initial velocities corresponding to 310K) were performed in the NpT ensemble with the Berendsen thermostat and Parrinello-Rahman barostat. The trajectories were sampled every 10 ps. The short run (1ns) of the equilibration was performed before the 100ns production run of each MD simulation.

Declarations

Acknowledgements

We thank Prof. Helena Žemličková and Dr. Václava Adámková for providing the strains for MIC testing, Mélanie Gillard for providing extensive training in the toeprinting assay, Dr. Zdeněk Lánský, and Doc. Ivan Hrdý for sharing their two ultracentrifuges, Dr. Martin Zoltner for sharing and helping with his CryoMill, Dr. Cyril Bařinka, and Doc. Jiří Petrák for sharing their two Typhoon Imaging Systems, Dr. Yuriy Petrenko for sharing his TECAN Infinite 200Pro reader, Prof. Reindert Nijland for gifting us the pRN12 plasmid, and Prof. Reynald Gillet for providing us the *E. coli* BW25113 Δ*tolC* strain.

This research was supported by the project National Institute of Virology and Bacteriology (Programme EXCELES, ID Project No. LX22NPO5103) – Funded by the European Union – Next Generation EU; by a grant from the Agence Nationale de la Recherche (ANR) (grant no. ANR-22-CE11-0012-01 RibioTiX); by a grant from the Programme Johannes Amos Comenius under the Ministry of Education, Youth and Sports of the Czech Republic (CZ.02.01.01/00/22_008/0004597); by the Ministry of Health of the Czech Republic (NU21-05- 00278 granted to Z.K. and M.Kr and NW25-09-00172 granted to M.Kr and G.B.N.); by the Technology Agency of the Czech Republic (TACR/8-11/2020 granted to J.J.); by the Grant Agency of Charles University (grant number 134324; granted to M.N.), and OP JAK—MSCA Fellowships CZ (CZ.02.01.01/00/22_010/0006118; granted to D.M.). The crystallographic part of this work was supported by the CzechNanoLab project LM2023051, funded by MEYS CR is gratefully acknowledge the financial support of the measurements/sample fabrication at LNSM Research Infrastructure.

Author contributions

G.B.N. designed the study. **M.N.**, **V.V.**, **J.P.**, and **M.B.** performed MIC testing. **M.N.**, **M.Ko.**, and **F.D.** purified different ribosome batches. **M.N.** performed toeprinting experiments, PEI assay, and prepared cryo-EM samples. **F.B.** and **M.N.** prepared cryo-EM grids. **F.B.** performed cryo-EM data collection. **M.N.** and **C.A.I.** processed cryo-EM data and built the models. **J.S.** and **M.N.** performed DNATCO model analysis. **D.Ř.** performed MD simulations. **F.D.** and **J.P.** prepared *S. aureus* extracts, and **F.D.** performed the TX-TL assay. **D.M.** and **T.S.** performed the binding assay. **G.B.N.** and **T.S.** performed the intracellular accumulation assay. **R.G.**, **P.S.**, **M.M.**, **J.H.**, and **K.Š.** synthesized ODC and CLC and performed quality control of intermediates. **M.Ku.** performed quality control of ODC and CLC. **V.E.** solved the solid-state X-ray structure of CLC. **L.H.** and **Z.K.** purified celesticetin. **G.B.N.**, **C.A.I.**, **J.J.**, **Z.K.**, and **M.Kr.** supervised the study. **J.J.**, **Z.K.**, **M.Kr.**, **G.B.N.**, **C.A.I.**, **D.M.**, and **M.N.** provided funding. **M.N.** wrote the first draft of the manuscript, and **G.B.N.** revised it. All authors revised the final draft of the manuscript. An AI-assisted language editing tool was used for copy editing and language refinement.

Competing interests

The authors R.G., Z.K., and J.J. are named inventors on patent applications WO2018161979 and US20200017537 “Lincosamide derivatives, preparation and use thereof as antimicrobial agent” filed by the Institute of Microbiology CAS, covering the lincosamide derivatives and their antimicrobial uses described in this study. All other authors declare no competing interests.

Data availability

Cryo-EM maps of the lincosamide-sensitive and lincosamide-resistant 70S–CLC complexes, along with the associated molecular models, have been deposited in the Electron Microscopy Data Bank and Protein Data Bank, with accession codes EMDB-52711 and PDB 9I88, and EMDB-52712 and PDB 9I89,

respectively. The X-ray structure of CLC has been deposited in the Cambridge Structural Database, with accession code CCDC 2529822.

References

1. Aleksandrova EV et al (2024) Macrolones target bacterial ribosomes and DNA gyrase and can evade resistance mechanisms. Nat Chem Biol 20:1680–1690
2. Bailey M et al (2008) Induction of erm(C) expression by noninducing antibiotics. Antimicrob Agents Chemother 52:866–874
3. Bayly CI et al (1993) A well-behaved electrostatic potential based method using charge restraints for deriving atomic charges: The RESP model. J Phys Chem 97:10269–10280
4. Berendsen HJC et al (1995) GROMACS: A message-passing parallel molecular dynamics implementation. Comput Phys Commun 91:43–56
5. Betteridge PW et al (2003) CRYSTALS version 12: software for guided crystal structure analysis. Urn:Issn:0021-8898 *36*, 1487–1487
6. Brandenburg K, Putz H (1999) DIAMOND
7. Buffie CG et al (2012) Profound alterations of intestinal microbiota following a single dose of clindamycin results in sustained susceptibility to Clostridium difficile-induced colitis. Infect Immun 80:62
8. Černý J et al (2020) A unified dinucleotide alphabet describing both RNA and DNA structures. Nucleic Acids Res 48:6367–6381
9. Černý J et al (2026) DNATCO v5.0: integrated web platform for 3D nucleic acid structure analysis. Nucleic Acids Res 54:gkaf1491
10. Collin MP et al (2009) Synthesis and evaluation of S- and C(1)-substituted analogues of lincomycin. Helv Chim Acta 92:230–266
11. Croll TI (2018) ISOLDE: A physically realistic environment for model building into low-resolution electron-density maps. Acta Crystallogr D Struct Biol 74:519–530
12. Crowe-McAuliffe C et al (2021) Structural basis of resistance to lincosamide, streptogramin A, and pleuromutilin antibiotics by ABCF ATPases in Gram-positive pathogens. Nat Commun *12*, 2020.11.24.396648.
13. DeBoer C et al (1955) Celesticetin - a new, crystalline antibiotic. I. Biological studies of celesticetin. Antibiot. Annu. *1954–1955*, 831–841
14. Douthwaite S (1992) Interaction of the antibiotics clindamycin and lincomycin with Escherichia coli 23S ribosomal RNA. Nucleic Acids Res 20:4717
15. Dunkle JA et al (2010) Structures of the Escherichia coli ribosome with antibiotics bound near the peptidyl transferase center explain spectra of drug action. Proc. Natl. Acad. Sci. U. S. A. *107*, 17152–17157

16. Emsley P et al (2010) Features and development of Coot. Acta Crystallogr D Biol Crystallogr 66:486–501
17. Eyal Z et al (2015) Structural insights into species-specific features of the ribosome from the pathogen Staphylococcus aureus. Proc. Natl. Acad. Sci. U. S. A. *112*, E5805–E5814
18. Fey PD et al (2013) A genetic resource for rapid and comprehensive phenotype screening of nonessential Staphylococcus aureus genes. MBio *4*, e00537-12
19. Gupta P et al (2013) Deregulation of translation due to post-transcriptional modification of rRNA explains why erm genes are inducible. Nat Commun 4:1–9
20. Hanada M et al (1980) Antibiotic Bu-2545, a new member of the celesticetin-lincomycin class. J Antibiot (Tokyo) 33:751–753
21. He M et al (2012) Emergence and global spread of epidemic healthcare-associated Clostridium difficile. Nature Genetics 2012 45:1 *45*, 109–113
22. Hoeksema H et al (1954) Isolation and purification of celesticetin. Antibiot. Annu. *1955*, 837–841
23. Hoeksema H et al (1964) Chemical studies on lincomycin. I. The structure of lincomycin. J Am Chem Soc 86:4223–4224
24. Hoeksema H (1968) Celesticetin. V. The structure of celesticetin. J Am Chem Soc 90:755–757
25. Iyer R et al (2018) Evaluating LC-MS/MS to measure accumulation of compounds within bacteria. ACS Infect Dis 4:1336–1345
26. Jang S (2023) AcrAB–TolC, a major efflux pump in Gram negative bacteria: toward understanding its operation mechanism. BMB Rep 56:326–334
27. Johnson S et al (1999) Epidemics of diarrhea caused by a clindamycin-resistant strain of Clostridium difficile in four hospitals. N Engl J Med 341:1645–1651
28. De Jong NWM et al (2017) Fluorescent reporters for markerless genomic integration in Staphylococcus aureus. Sci Rep *7*
29. Kadlčík S et al (2017) Elucidation of salicylate attachment in celesticetin biosynthesis opens the door to create a library of more efficient hybrid lincosamide antibiotics. Chem Sci 8:3349–3355
30. Kimanius D et al (2021) New tools for automated cryo-EM single-particle analysis in RELION-4.0. Biochem J 478:4169–4185
31. Knight DR et al (2021) Major genetic discontinuity and novel toxigenic species in Clostridioides difficile taxonomy. Elife *10*
32. Krůtová M et al (2025) Genomic islands and molecular mechanisms relating to drug-resistance in Clostridioides (Clostridium) difficile PCR ribotype 176. Emerg. Microbes Infect. *14*
33. Kuijper EJ et al (2001) Nosocomial outbreak of Clostridium difficile-associated diarrhoea due to a clindamycin-resistant enterotoxin A-negative strain. Eur J Clin Microbiol Infect Dis 20:528–534
34. Kwon YC, Jewett MC (2015) High-throughput preparation methods of crude extract for robust cell-free protein synthesis. Sci Rep 5:1–8

35. Leclercq R, Courvalin P (1991) Bacterial resistance to macrolide, lincosamide, and streptogramin antibiotics by target modification. Antimicrob Agents Chemother 35:1267–1272
36. Liebschner D et al (2019) Macromolecular structure determination using X-rays, neutrons and electrons: recent developments in Phenix. Acta Crystallogr D Struct Biol 75:861
37. Lindahl E et al (2001) GROMACS 3.0: A package for molecular simulation and trajectory analysis. J Mol Model 7:306–317
38. Magerlein BJ (1971) Modification of lincomycin. Adv Appl Microbiol 14:185–229
39. Matzov D et al (2017) Structural insights of lincosamides targeting the ribosome of Staphylococcus aureus. Nucleic Acids Res 45:10284–10292
40. Meng EC et al (2023) UCSF ChimeraX: Tools for structure building and analysis. Protein Sci 32:e4792
41. Mitcheltree MJ et al (2021) A synthetic antibiotic class overcoming bacterial multidrug resistance. Nature 599:507–512
42. Najmanová L et al (2014) Sequence analysis of porothramycin biosynthetic gene cluster. Folia Microbiol (Praha) 59:543
43. Obana N et al (2023) Genome-encoded ABCF factors implicated in intrinsic antibiotic resistance in Gram-positive bacteria: VmlR2, Ard1 and CplR. Nucleic Acids Res 51:4536
44. Orelle C et al (2013) Tools for characterizing bacterial protein synthesis inhibitors. Antimicrob Agents Chemother 57:5994–6004
45. Palatinus L, Chapuis G (2007) SUPERFLIP – a computer program for the solution of crystal structures by charge flipping in arbitrary dimensions. Urn:Issn:0021-8898 *40*, 786–790
46. Paternoga H et al (2023) Structural conservation of antibiotic interaction with ribosomes. Nat Struct Mol Biol 1–13
47. Pear SM et al (2000) Decrease in nosocomial Clostridium difficile–associated diarrhea by restricting clindamycin use. Https://Doi Org/ 120272–277. 10.7326/0003-4819-120-4-199402150-00003
48. Pérez A et al (2007) Cloning, nucleotide sequencing, and analysis of the AcrAB-TolC efflux pump of Enterobacter cloacae and determination of its involvement in antibiotic resistance in a clinical isolate. Antimicrob Agents Chemother 51:3247–3253
49. Pettersen EF et al (2004) UCSF Chimera—A visualization system for exploratory research and analysis. J Comput Chem 25:1605–1612
50. Plankaová A et al (2023) Clostridioides difficile infections were predominantly driven by fluoroquinolone-resistant Clostridioides difficile ribotypes 176 and 001 in Slovakia in 2018–2019. Int. J. Antimicrob. Agents *62*
51. Punjani A et al (2017) cryoSPARC: algorithms for rapid unsupervised cryo-EM structure determination. Nat Methods 14:290–296
52. Rohlíček J, Hušák M (2007) MCE2005 – a new version of a program for fast interactive visualization of electron and similar density maps optimized for small molecules. Urn:Issn:0021-8898 *40*, 600–

601
53. Rohou A, Grigorieff N (2015) CTFFIND4: Fast and accurate defocus estimation from electron micrographs. J Struct Biol 192:216–221
54. Schindler BD, Kaatz GW (2016) Multidrug efflux pumps of Gram-positive bacteria. Drug Resist Updates 27:1–13
55. Schlünzen F et al (2001) Structural basis for the interaction of antibiotics with the peptidyl transferase centre in eubacteria. Nature 413:814–821
56. Seip B et al (2018) Ribosomal stalling landscapes revealed by high-throughput inverse toeprinting of mRNA libraries. Life Sci. Alliance *1*
57. Sharkey LKR et al (2016) ABC-F proteins mediate antibiotic resistance through ribosomal protection. MBio *7*, e01975-15
58. Silverman AD et al (2019) Deconstructing cell-free extract preparation for in vitro activation of transcriptional genetic circuitry. ACS Synth Biol 8:403–414
59. Van Der Spoel D et al (2005) GROMACS: Fast, flexible, and free. J Comput Chem 26:1701–1718
60. Šponer J et al (2014) Molecular dynamics simulations of nucleic acids. From tetranucleotides to the ribosome. J Phys Chem Lett 5:1771–1782
61. Toh SM et al (2007) Acquisition of a natural resistance gene renders a clinical strain of methicillin-resistant Staphylococcus aureus resistant to the synthetic antibiotic linezolid. Mol Microbiol 64:1506–1514
62. Tu D et al (2005) Structures of MLSBK antibiotics bound to mutated large ribosomal subunits provide a structural explanation for resistance. Cell 121:257–270
63. Wang J et al (2004) Development and testing of a general amber force field. J Comput Chem 25:1157–1174
64. World Health Organization (2023) Antimicrobial resistance [Fact sheet]
65. Wu KJY et al (2024) An antibiotic preorganized for ribosomal binding overcomes antimicrobial resistance. Science (1979). *383*, 721–726
66. Zheng SQ et al (2017) MotionCor2: anisotropic correction of beam-induced motion for improved cryo-electron microscopy. Nat Methods 14:331–332
67. Zíková J et al (2025) Newly emerging metronidazole-resistant Clostridioides difficile PCR ribotype 955 identified in Poland, 2021 to 2023 but not in Czechia, 2012 to 2023 and Slovakia, 2015 to 2023. Euro Surveill. *30*

Figures

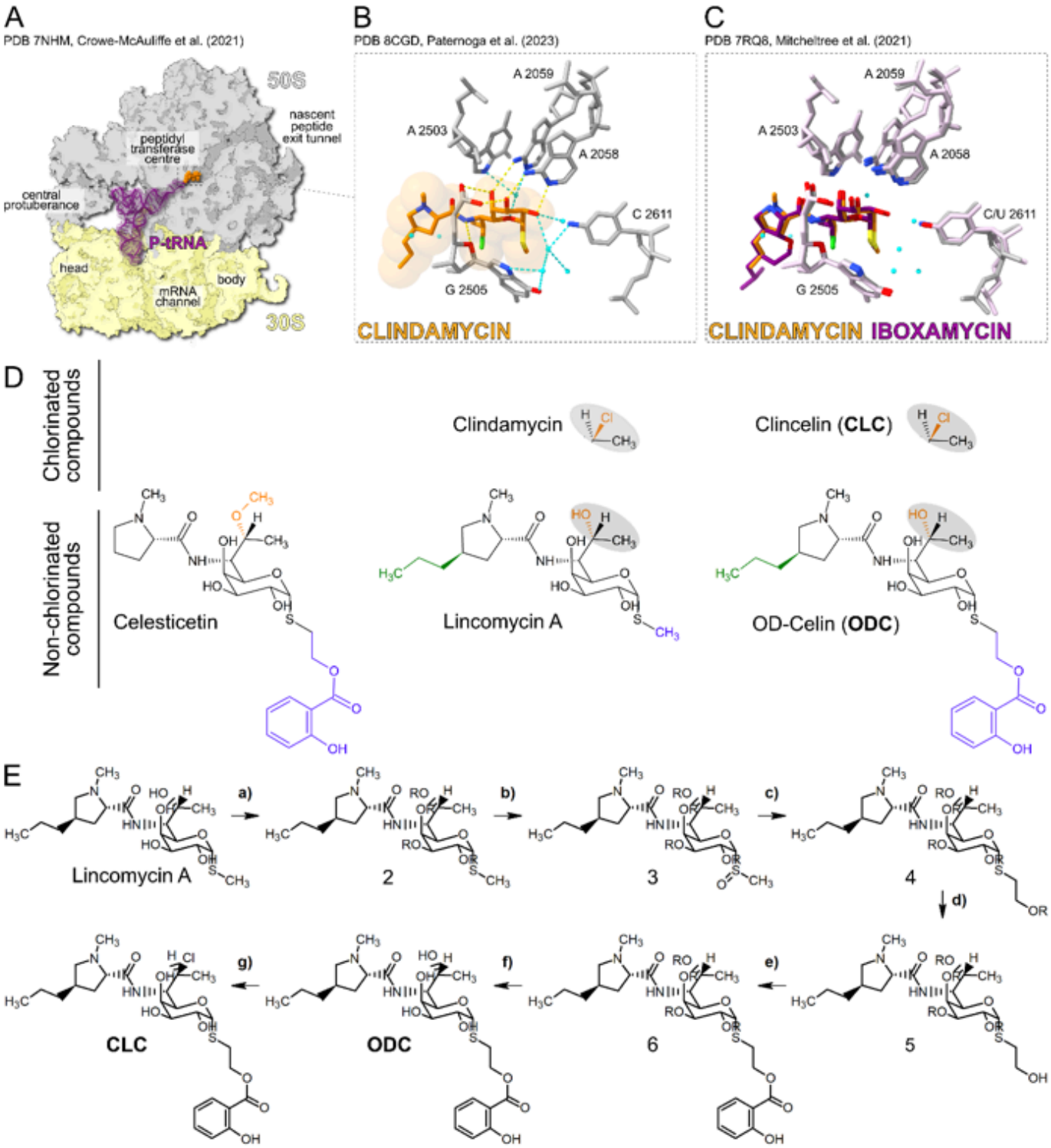


Figure 1

Structure, binding site, and synthesis of lincosamides. (**A**) Overview of the *S. aureus* 70S ribosome consisting of the large 50S subunit (grey) and small 30S subunit (yellow; PDB 7NHM) (Crowe-McAuliffe et al., 2021). (**B**) A detailed view of the clindamycin (dark orange) binding pocket within the 50S subunit of the *Escherichia coli* (*E. coli*) ribosome (grey; PDB 8CGD) (Paternoga et al., 2023). The hydrogen bond network formed by the nucleotides of the 23S rRNA is shown in yellow, and the coordinated water

molecules are depicted in cyan (PDB 8CGD). (**C**) Superposition of ribosome-bound clindamycin (gold) from panel B and iboxamycin (purple) in complex with *Thermus thermophilus* ribosome (thistle; PDB 7RQ8) (Mitcheltree et al., 2021). (**D**) Chemical structures of two natural antibiotics, celesticetin and lincomycin A, and their semi-synthetic derivatives, clindamycin, ODC, and CLC. ODC is an unnatural chimera of celesticetin and lincomycin. CLC is a chlorinated derivative of ODC. Different colors highlight the structural differences among the compounds: the 4-propyl side chain (green), the chlorine/hydroxy group (orange), and the salicylate moiety (blue). (**E**) Scheme of CLC synthesis. The intermediates are indicated as compounds 2-6. R = TBDMS. a) TBDMSOTf, Pyridine, 110 °C; b) i. mCPBA, DCM, 0 °C; ii. $(PinB)_2$, MeCN/Et_2O, r.t.; c) $HSCH_2CH_2OTBDMS$, DTBMP, Tf_2O, Et_2O, -78 °C to 0 °C; d) TFA/H_2O, THF, 0 °C; e) Salicylic acid, DCC, DMAP, DCM, r.t.; f) TBAF·$3H_2O$, THF, r.t.; g) i. $(COCl)_2$, DMF, 63 °C; ii. K_2CO_3 (aq.), 0 °C.

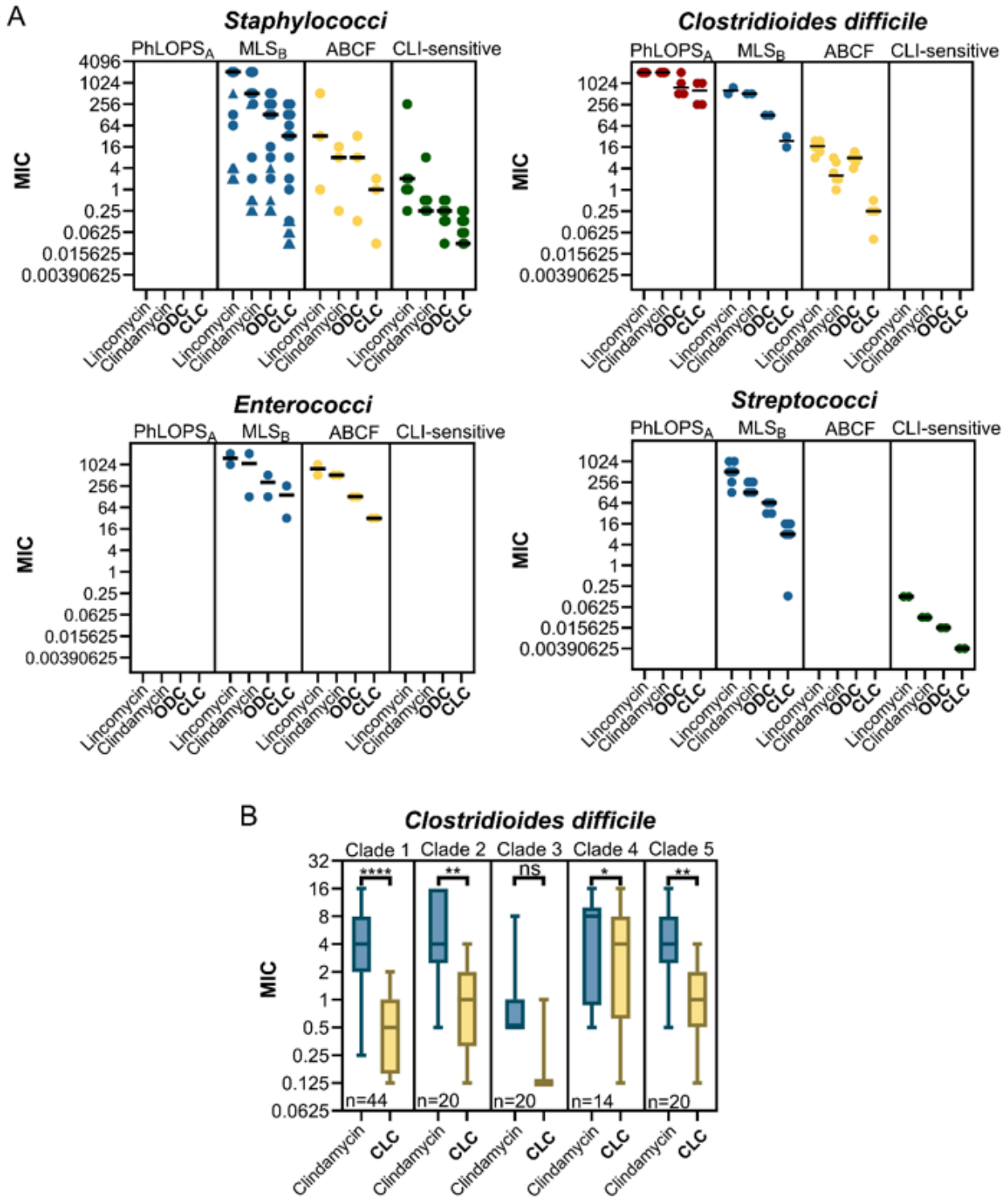


Figure 2

Antimicrobial activity of new and established lincosamides against Gram-positive pathogens. (**A**) Minimum inhibitory concentrations (MICs) of lincomycin, clindamycin, ODC, and CLC against representative clinical isolates of *Staphylococci* (n=43), *Clostridioides difficile* (n=12), *Enterococci* (n=4), and *Streptococci* (n=10) with defined clindamycin-resistance mechanisms. Data are grouped by resistance mechanism: PhLOPS$_A$ (phenicol-lincosamide-oxazolidinone-pleuromutilin-streptogramin A

resistance), MLS_B
(macrolide-lincosamide-streptogramin B resistance), ABCF-mediated resistance, and clindamycin-sensitive strains. Each dot represents an individual isolate, and the horizontal bars indicate the median MIC. A triangle marks strains with inducible MLS_B resistance. Full datasets are provided in Supplementary Fig. 2. (**B**) Clade-specific MIC distributions of clindamycin and CLC in *C. difficile*. MICs were determined for strains with intrinsic, ABC-F–mediated resistance to clindamycin. CLC showed consistently lower MICs than clindamycin across all clades (1–5). Box plots depict median, interquartile range, and minimum/maximum values. Statistical comparisons between clindamycin and CLC within each clade were performed using the Welch Two Sample t-test, with *p*-values adjusted for multiple comparisons using the Bonferroni method. Significance is indicated as $p \leq 0.05$, **$p \leq 0.01$, ***$p \leq 0.001$, and ****$p \leq 0.0001$ (adjusted).

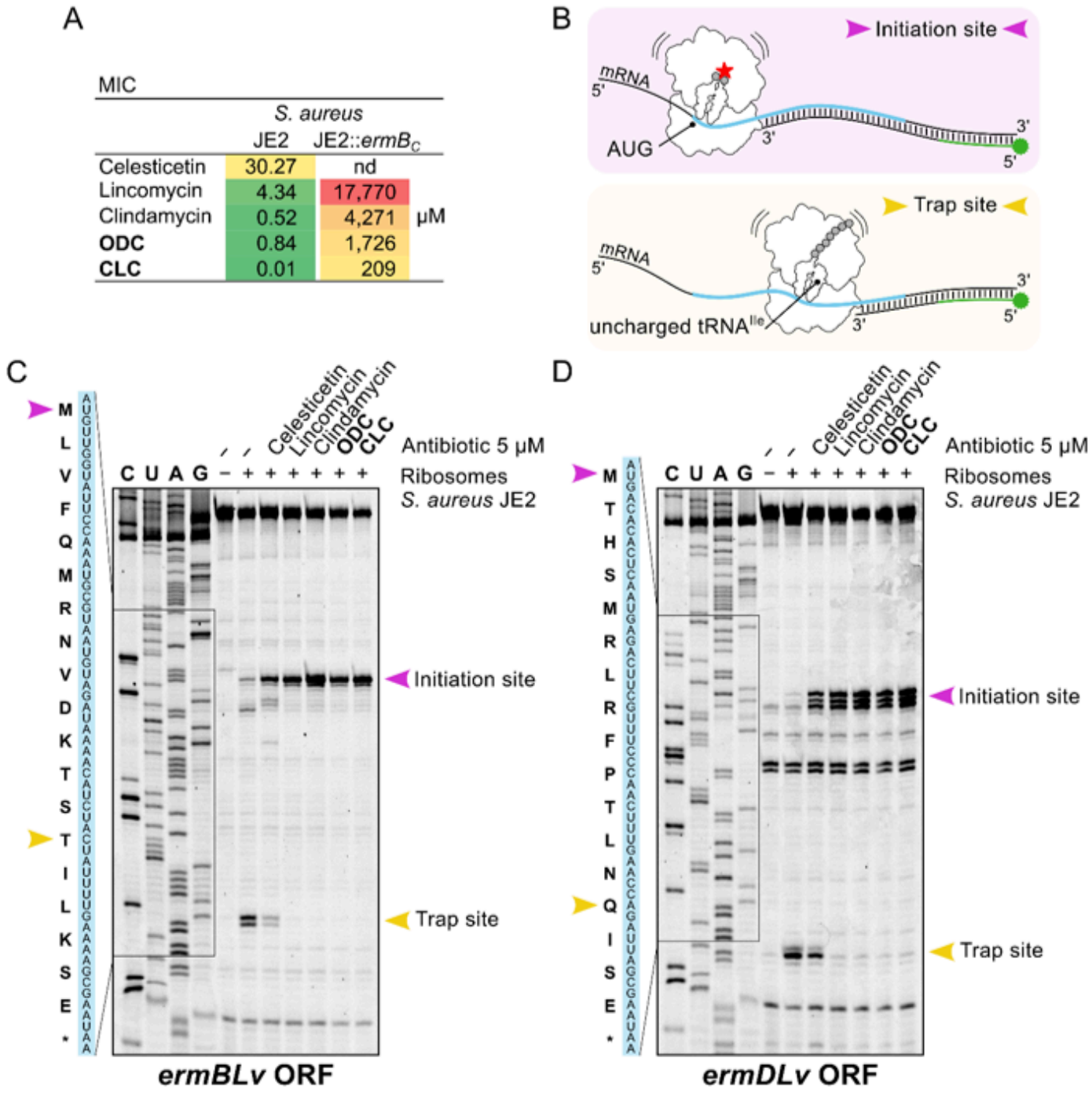


Figure 3

***In vitro* activity testing of lincosamide antibiotics.** (**A**) Minimal inhibitory concentration (µM) of lincosamides against *Staphylococcus aureus* JE2 and JE2 constitutively expressing methyltransferase ErmB (JE2::*ermB*$_C$; NE1858), which were used as parental strains for *in vitro* tests throughout this study, unless otherwise stated. (**B**) Toeprinting assay concept: Ribosomes are stalled either by an antibiotic (magenta) or trapped due to the presence of uncharged tRNA^{Ile} (yellow). The position of arrested ribosomes is identified by reverse transcription of mRNA using a fluorescently labeled primer (green). (**C**, **D**) Toeprinting analysis of lincosamide-dependent stalling of ribosomes translating variants of *ermBL* (**C**)

and *ermDL* (**D**). All tested lincosamide antibiotics cause stalling of the ribosome at 5 µM concentration when the start codon is in the ribosomal P-site (magenta arrow).

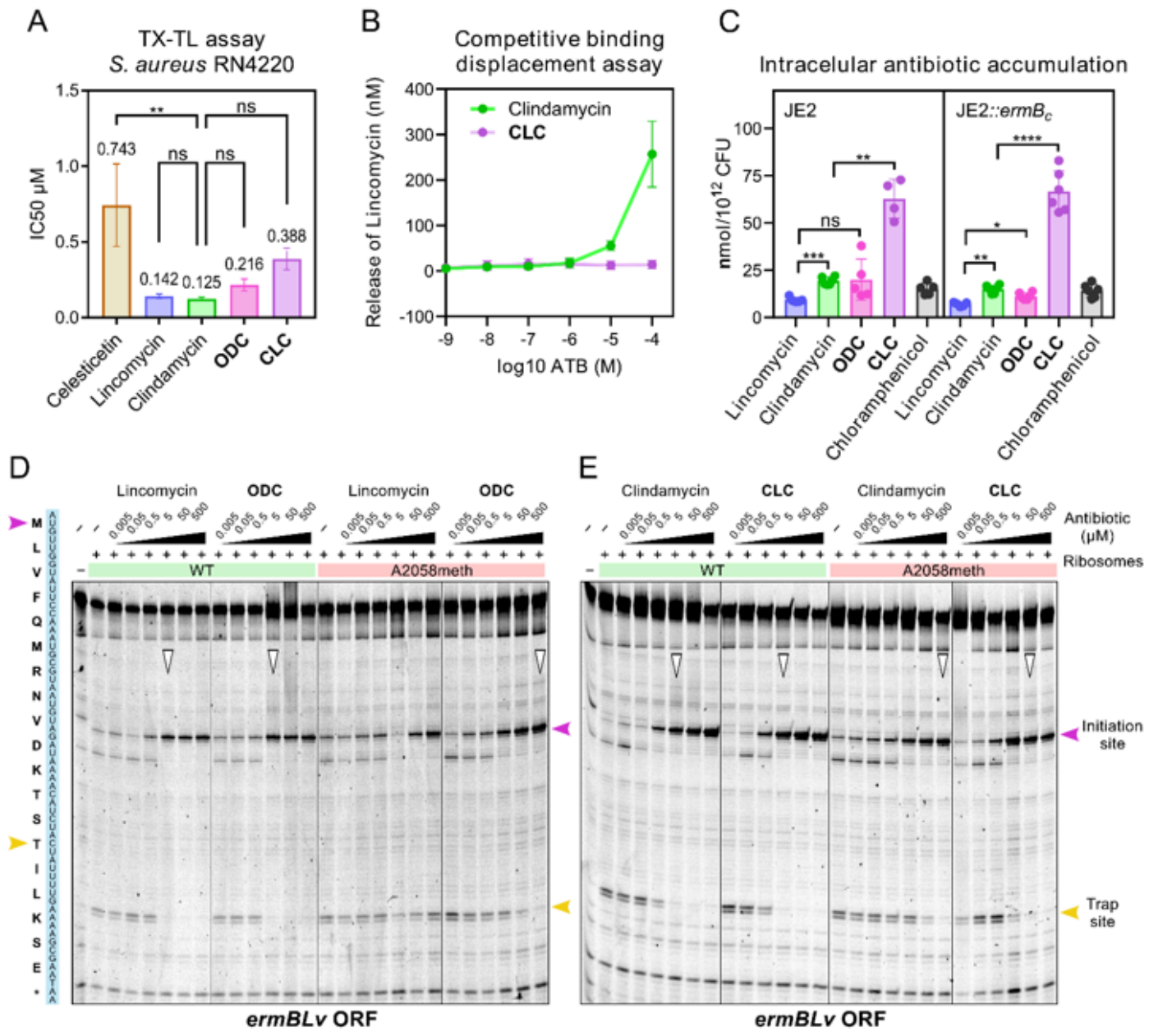


Figure 4

***In vitro* assays deciphering a detailed mechanism of enhanced antimicrobial activity of CLC.** (**A**) The half-maximal inhibitory concentration (IC50) for celesticetin, lincomycin, clindamycin, ODC, and CLC was quantified using an 8-hour *S. aureus* RN4220 cell-free transcription-translation (TX-TL) assay. IC 50 values were derived from concentration-response curves using a four-parameter logistic (4PL) model. Data points represent the mean ± SD of four independent experiments. . Statistical comparison of IC 50 values was performed by One-way ANOVA followed by Tukey's multiple comparisons test (ns: not significant, ∗∗ for p<0.01). (**B**) Competitive displacement of unlabeled lincomycin from isolated *S. aureus* JE2 ribosomes by increasing concentrations of clindamycin and CLC. Lincomycin released from

ribosomes was quantified by LC-MS. (**C**) Intracellular accumulation (six biological replicates in two independent experiments) measured in lincosamide-sensitive *S. aureus* JE2 and lincosamide-resistant derivative JE2::*ermB*$_C$ (strain NE854) showed that CLC achieves superior uptake compared to lincomycin, clindamycin, and ODC in both strains. Chloramphenicol was included as a positive control for cellular uptake. Statistical significance was assessed using a paired, two-tailed Student's t-test: ns (not significant), ∗ for p<0.05, ∗∗ for p<0.01, ∗∗∗ for p<0.001, ∗∗∗∗ for p<0.0001 (**D**, **E**). Toeprinting assays with *S. aureus* ribosomes show comparable inhibition by lincomycin and ODC (**D**), and clindamycin and CLC (**E**) at 5 μM on sensitive ribosomes. On A2058-dimethylated ribosomes (~60% of the population methylated; as determined by primer extension inhibition assay; Extended Data Fig. 6C), lincomycin failed to fully inhibit translation even at 500 μM, whereas clindamycin and ODC did so at this concentration. CLC achieved complete inhibition at 50 μM only. White arrows mark the minimal fully inhibitory concentration. The toeprinting assay concept is explained in Fig. 3B.

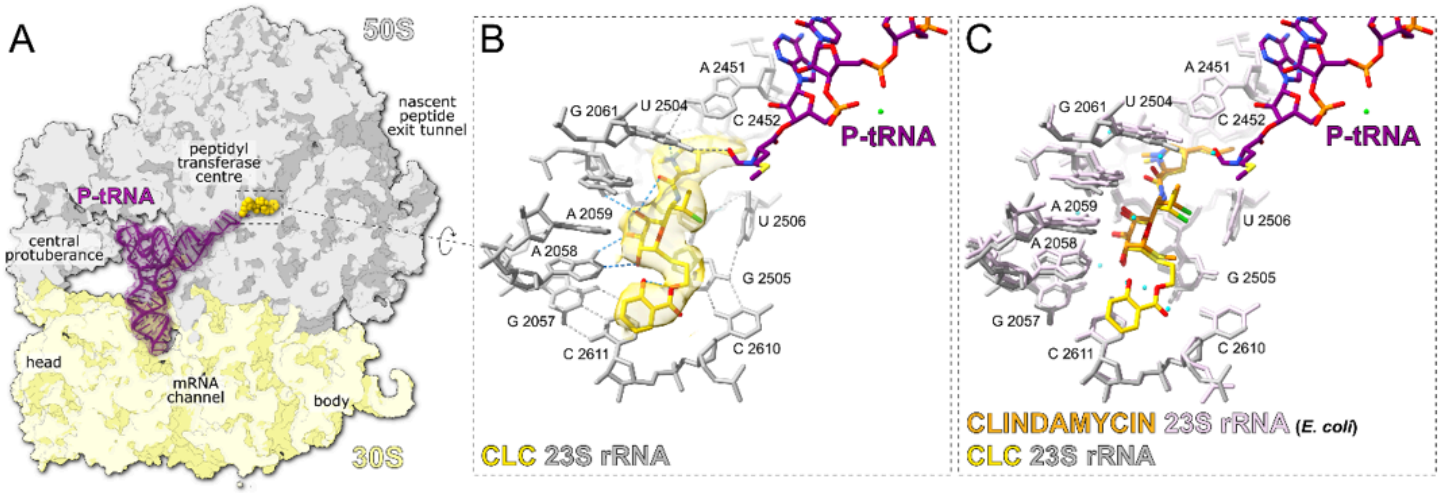


Figure 5

Cryo-EM structure of CLC bound to 70S *S. aureus* ribosome with P-tRNA. (**A**) *S. aureus* 70S ribosome: 30S subunit (yellow), 50S subunit (grey), P-site tRNA (purple), and CLC (gold) are shown. (**B**) Detailed view of the CLC (gold) binding pocket. Interactions with the nucleotides of 23S rRNA are indicated as blue dashed lines. A sharpened Coulomb potential map is shown using a surface representation. (**C**) Superposition of CLC (gold) in complex with *S. aureus* ribosome (grey) and clindamycin (dark orange) in complex with *E. coli* ribosome (thistle; PDB 8CGD) (Paternoga et al., 2023).

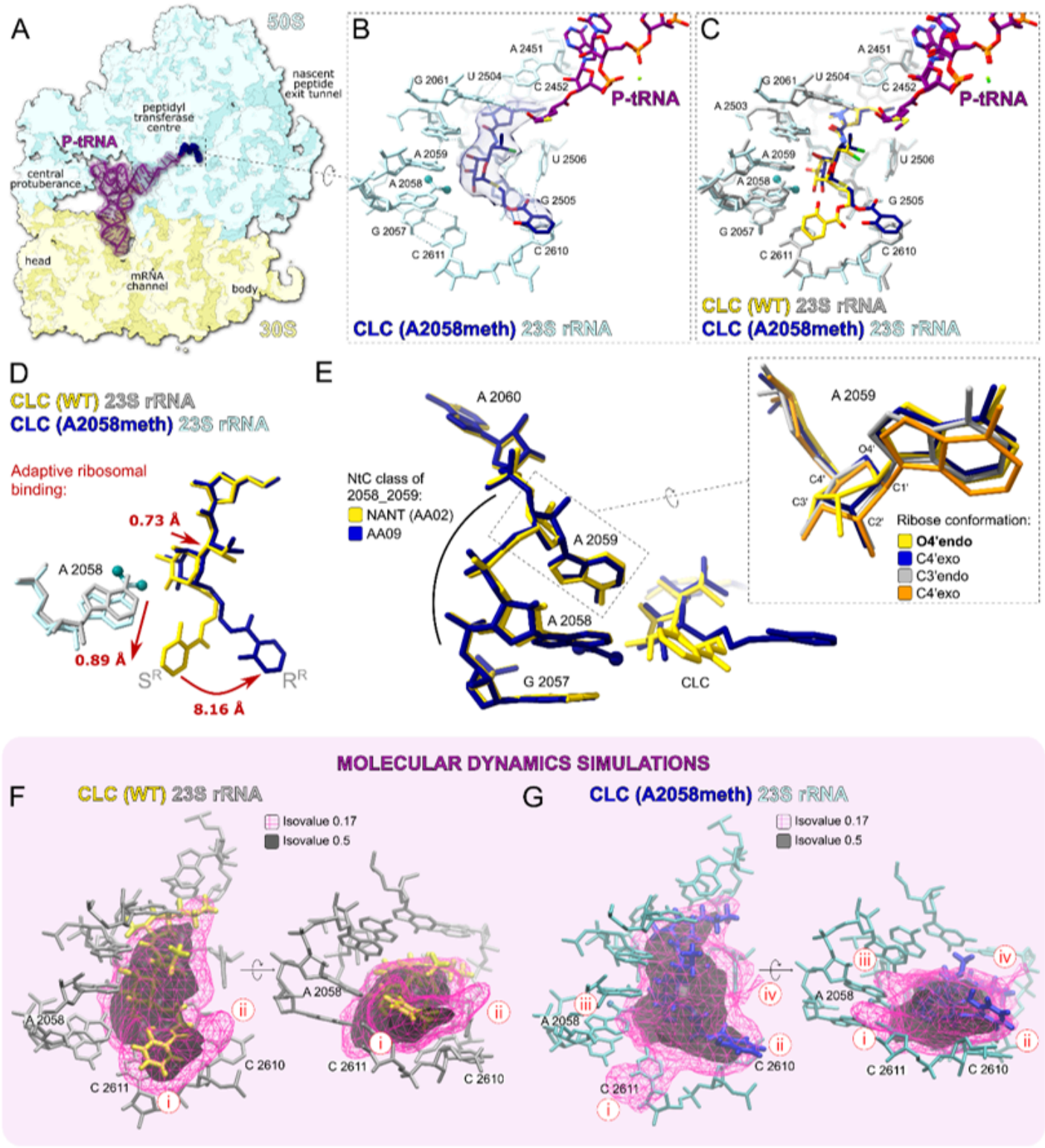


Figure 6

Cryo-EM structure of CLC bound to the *S. aureus* A2058-dimethylated 70S ribosome with bound P-tRNA. (**A**) *S. aureus* 70S ribosome: 30S subunit (yellow), 50S subunit (powder blue), P-site tRNA (purple), and CLC (navy blue) are shown. (**B**) Detailed view of the CLC (navy blue) binding pocket. The two methyl groups of A2058, shown as spheres, are highlighted in teal. A sharpened density map is shown as a surface. (**C**) Superposition of CLC (gold) in complex with non-methylated *S. aureus* ribosome (grey) and

CLC (navy blue) in complex with A2058-dimethylated *S. aureus* ribosome (powder blue). (**D**) Despite the presence of resistance methylation, CLC's adaptive structural flexibility allows antibiotic binding to the ribosome. This anti-resistance adaptation involves the movement of the methylated nucleotide and the switch of the antibiotic conformation from S^R to R^R. (**E**) CLC-induced conformational remodeling of the A2058_A2059 dinucleotide step within the 23S rRNA of the lincosamide-sensitive ribosome. As characterized by DNATCO (Černý et al., 2020, 2026), CLC in its S^R conformation promotes a structural rearrangement of the A2058_A2059 dinucleotide, manifested by a transition in the A2059 ribose conformation. Shown is a superposition of CLC bound to the lincosamide-sensitive ribosome (gold) and to the A2058-dimethylated ribosome (navy blue). In the focus panel, a vacant *S. aureus* ribosome (grey; PDB 4WCE) (Eyal et al., 2015) and a clindamycin-bound *E. coli* ribosome (orange; PDB 8CGD) (Paternoga et al., 2023) are additionally superimposed. NANT – non-assigned dinucleotide (the closest NtC class is indicated in brackets). (**F**, **G**) Molecular dynamics simulation showed high-level flexibility and dynamics of the salicylate moiety in both models. Artificially generated density maps, displayed at two different isovalue levels in VMD v2.0.0a7, retain the position of CLC throughout the simulation (three 100-ns-long simulations concatenated into one – 1879 frames per sample). The molecular models shown are the starting models of the simulation, derived from the experimental cryo-EM structures (PDB 9I88 and 9I89, respectively). Alternative electron densities are labeled **i**–**ii** in the lincosamide-sensitive ribosome (**F**) and **i**–**iv** in the lincosamide-resistant ribosome (**G**), with the Roman numerals in both models indicating electron density clouds occupying equivalent spatial positions.

Supplementary Files

This is a list of supplementary files associated with this preprint. Click to download.

- MovieS1sensitiveriborep1.mp4
- MovieS2sensitiveriborep2.mp4
- MovieS3sensitiveriborep3.mp4
- MovieS4resistantriborep1.mp4
- MovieS5resistantriborep2.mp4
- MovieS6resistantriborep3.mp4
- GA.png
- SourceDataFigs24andExDataFigs56.xlsx
- SupplementaryInformation.docx
- GA.png
- ExtendedDataFig.docx